Maksym, WP, Liodakis, I, Saade, ML, Kim, DE, Middei, R, Di Gesu, L, Kiehlmann, S, Matzeu, G, Agudo, I, Marscher, AP, Ehlert, SR, Jorstad, SG, Kaaret, P, Marshall, HL, Pacciani, L, Perri, M, Puccetti, S, Kouch, PM, Lindfors, E, Aceituno, FJ, Bonnoli, G, Casanova, V, Escudero, J, Gómez, JL, Agís-González, B, Husillos, C, Morcuende, D, Otero-Santos, J, Sota, A, Piirola, V, Imazawa, R, Sasada, M, Fukazawa, Y, Kawabata, KS, Uemura, M, Mizuno, T, Nakaoka, T, Akitaya, H, McCall, C, Jermak, HE, Steele, IA, Borman, GA, Grishina, TS, Hagen-Thorn, VA, Kopatskaya, EN, Larionova, EG, Morozova, DA, Savchenko, SS, Shishkina, EV, Troitskiy, IS, Troitskaya, YV, Vasilyev, AA, Zhovtan, AV, Myserlis, I, Gurwell, M, Keating, G, Rao, R, Pauley, C, Angelakis, E, Kraus, A, Berdyugin, AV, Kagitani, M, Kravtsov, V, Poutanen, J, Sakanoi, T, Kang, S, Lee, S-S, Kim, S-H, Cheong, WY, Jeong, H-W, Song, C, Blinov, D, Shablovinskaya, E, Antonelli, LA, Bachetti, M, Baldini, L, Baumgartner, WH, Bellazzini, R, Bianchi, S, Bongiorno, SD, Bonino, R, Brez, A, Bucciantini, N, Capitanio, F, Castellano, S, Cavazzuti, E, Chen, C-T, Ciprini, S, Costa, E, De Rosa, A, Del Monte, E, Di Lalla, N, Di Marco, A, Donnarumma, I, Doroshenko, V, Dovčiak, M, Enoto, T, Evangelista, Y, Fabiani, S, Ferrazzoli, R, Garcia, JA, Gunji, S, Hayashida, K, Heyl, J, Iwakiri, W, Karas, V, Kislat, F, Kitaguchi, T, Kolodziejczak, JJ, Krawczynski, H, La Monaca, F, Latronico, L, Maldera, S, Manfreda, A, Marin, F, Marinucci, A, Massaro, F, Matt, G, Mitsuishi, I, Muleri, F, Negro, M, Ng, C-Y, O'Dell, SL, Omodei, N, Oppedisano, C, Papitto, A, Pavlov, GG, Peirson, AL, Pesce-Rollins, M, Petrucci, P-O, Pilia, M, Possenti, A, Ramsey, BD, Rankin, J, Ratheesh, A, Roberts, OJ, Romani, RW, Sgró, C, Slane, P, Soffitta, P, Spandre, G, Swartz, DA, Tamagawa, T, Tavecchio, F, Taverna, R, Tawara, Y, Tennant, AF, Thomas, NE, Tombesi, F, Trois, A, Tsygankov, SS, Turolla, R, Vink, J, Weisskopf, MC, Wu, K, Xie, F and Zane, S

A Two-week IXPE Monitoring Campaign on Mrk 421

The Astrophysical Journal, 986:230 (20pp), 2025 June 20 https://doi.org/10.3847/1538-4357/adce6b

A Two-week IXPE Monitoring Campaign on Mrk 421

W. Peter Maksym[1], Ioannis Liodakis[1,2], M. Lynne Saade[1,3], Dawoon E. Kim[4,5,6], Riccardo Middei[4], Laura Di Gesu[7], Sebastian Kiehlmann[2,8], Gabriele Matzeu[9], Iván Agudo[10], Alan P. Marscher[11], Steven R. Ehlert[1], Svetlana G. Jorstad[11,12], Philip Kaaret[1], Herman L. Marshall[13], Luigi Pacciani[4], Matteo Perri[14,15], Simonetta Puccetti[14], Pouya M. Kouch[16,17,18], Elina Lindfors[16], Francisco José Aceituno[10], Giacomo Bonnoli[10,19], Víctor Casanova[10], Juan Escudero[10], José L. Gómez[10], Beatriz Agís-González[2], César Husillos[10,20], Daniel Morcuende[10], Jorge Otero- Santos[10], Alfredo Sota[10], Vilppu Piirola[16], Ryo Imazawa[21], Mahito Sasada[22], Yasushi Fukazawa[21,23,24], Koji S. Kawabata[21,23,24], Makoto Uemura[21,23,24], Tsunefumi Mizuno[23], Tatsuya Nakaoka[23], Hiroshi Akitaya[25], Callum McCall[26], Helen E. Jermak[26], Iain A. Steele[26], George A. Borman[27], Tatiana S. Grishina[12], Vladimir A. Hagen-Thorn[12], Evgenia N. Kopatskaya[12], Elena G. Larionova[12], Daria A. Morozova[12], Sergey S. Savchenko[12,28,29], Ekaterina V. Shishkina[12], Ivan S. Troitskiy[12], Yulia V. Troitskaya[12], Andrey A. Vasilyev[12], Alexey V. Zhovtan[27], Ioannis Myserlis[30,31], Mark Gurwell[32], Garrett Keating[32], Ramprasad Rao[32], Colt Pauley[33], Emmanouil Angelakis[34], Alexander Kraus[31], Andrei V. Berdyugin[16], Masato Kagitani[35], Vadim Kravtsov[16], Juri Poutanen[16], Takeshi Sakanoi[35], Sincheol Kang[36], Sang-Sung Lee[36,37], Sang-Hyun Kim[36,37], Whee Yeon Cheong[36,37], Hyeon-Woo Jeong[36,37], Chanwoo Song[36,37], Dmitry Blinov[2,8], Elena Shablovinskaya[38,39], Lucio Angelo Antonelli[14,15], Matteo Bachetti[40], Luca Baldini[41,42], Wayne H. Baumgartner[1], Ronaldo Bellazzini[41], Stefano Bianchi[43], Stephen D. Bongiorno[1], Raffaella Bonino[44,45], Alessandro Brez[41], Niccoló Bucciantini[46,47,48], Fiamma Capitanio[4], Simone Castellano[41], Elisabetta Cavazzuti[7], Chien-Ting Chen[49], Stefano Ciprini[14,50], Enrico Costa[4], Alessandra De Rosa[4], Ettore Del Monte[4], Niccoló Di Lalla[51], Alessandro Di Marco[4], Immacolata Donnarumma[7], Victor Doroshenko[52], Michal Dovčiak[53], Teruaki Enoto[54], Yuri Evangelista[4], Sergio Fabiani[4], Riccardo Ferrazzoli[4], Javier A. Garcia[55], Shuichi Gunji[56], Kiyoshi Hayashida[57], Jeremy Heyl[58], Wataru Iwakiri[59], Vladimir Karas[53], Fabian Kislat[60], Takao Kitaguchi[54], Jeffery J. Kolodziejczak[1], Henric Krawczynski[61], Fabio La Monaca[4,5,6], Luca Latronico[44], Simone Maldera[44], Alberto Manfreda[62], Frédéric Marin[63], Andrea Marinucci[7], Francesco Massaro[44,45], Giorgio Matt[43], Ikuyuki Mitsuishi[64], Fabio Muleri[4], Michela Negro[65], C.-Y. Ng[66], Stephen L. O'Dell[1], Nicola Omodei[51], Chiara Oppedisano[44], Alessandro Papitto[15], George G. Pavlov[67], Abel Lawrence Peirson[51], Melissa Pesce-Rollins[41], Pierre-Olivier Petrucci[68], Maura Pilia[40], Andrea Possenti[40], Brian D. Ramsey[1], John Rankin[4], Ajay Ratheesh[4], Oliver J. Roberts[49], Roger W. Romani[51], Carmelo Sgró[41], Patrick Slane[32], Paolo Soffitta[4], Gloria Spandre[41], Douglas A. Swartz[49], Toru Tamagawa[54], Fabrizio Tavecchio[19], Roberto Taverna[69], Yuzuru Tawara[64], Allyn F. Tennant[1], Nicholas E. Thomas[1], Francesco Tombesi[6,50], Alessio Trois[40], Sergey S. Tsygankov[16], Roberto Turolla[69,70], Jacco Vink[71], Martin C. Weisskopf[1], Kinwah Wu[70], Fei Xie[4,72], and Silvia Zane[70]

[1] NASA Marshall Space Flight Center, Huntsville, AL 35812, USA
[2] Institute of Astrophysics, Foundation for Research and Technology-Hellas, GR-70013 Heraklion, Greece
[3] Science & Technology Institute, Universities Space Research Association, 320 Sparkman Drive, Huntsville, AL 35805, USA
[4] INAF Istituto di Astrofisica e Planetologia Spaziali, Via del Fosso del Cavaliere 100, 00133 Roma, Italy
[5] Dipartimento di Fisica, Universitá degli Studi di Roma "La Sapienza," Piazzale Aldo Moro 5, 00185 Roma, Italy
[6] Dipartimento di Fisica, Universitá degli Studi di Roma "Tor Vergata," Via della Ricerca Scientifica 1, 00133 Roma, Italy
[7] ASI—Agenzia Spaziale Italiana, Via del Politecnico snc, 00133 Roma, Italy
[8] Department of Physics, University of Crete, GR-70013 Heraklion, Greece
[9] G. A. Matzeu—Quasar Science Resources SL for ESA, European Space Astronomy Centre (ESAC), Science Operations Department, 28692, Villanueva de la Cañada, Madrid, Spain
[10] Instituto de Astrofísica de Andalucía, IAA-CSIC, Glorieta de la Astronomía s/n, 18008 Granada, Spain
[11] Institute for Astrophysical Research, Boston University, 725 Commonwealth Avenue, Boston, MA 02215, USA
[12] Saint Petersburg State University, 7/9 Universitetskaya nab., St. Petersburg, 199034, Russia
[13] MIT Kavli Institute for Astrophysics and Space Research, Massachusetts Institute of Technology, 77 Massachusetts Avenue, Cambridge, MA 02139, USA
[14] Space Science Data Center, Agenzia Spaziale Italiana, Via del Politecnico snc, 00133 Roma, Italy
[15] INAF Osservatorio Astronomico di Roma, Via Frascati 33, 00078 Monte Porzio Catone (RM), Italy
[16] Department of Physics and Astronomy, 20014, University of Turku, Finland
[17] Finnish Centre for Astronomy with ESO, 20014, University of Turku, Finland
[18] Aalto University Metsähovi Radio Observatory, Metsähovintie 114, FI-02540 Kylmälä, Finland
[19] INAF Osservatorio Astronomico di Brera, Via E. Bianchi 46, 23807 Merate (LC), Italy
[20] Geological and Mining Institute of Spain (IGME), CSIC, Calle Ríos Rosas 23, 28003 Madrid, Spain
[21] Department of Physics, Graduate School of Advanced Science and Engineering, Hiroshima University Kagamiyama, 1-3-1 Higashi-Hiroshima, Hiroshima 739-8526, Japan
[22] Department of Physics, Tokyo Institute of Technology, 2-12-1 Ookayama, Meguro-ku, Tokyo 152-8551, Japan
[23] Hiroshima Astrophysical Science Center, Hiroshima University 1-3-1 Kagamiyama, Higashi-Hiroshima, Hiroshima 739-8526, Japan
[24] Core Research for Energetic Universe (Core-U), Hiroshima University, 1-3-1 Kagamiyama, Higashi-Hiroshima, Hiroshima 739-8526, Japan
[25] Astronomy Research Center, Chiba Institute of Technology, 2-17-1 Tsudanuma, Narashino, Chiba 275-0016, Japan
[26] Astrophysics Research Institute, Liverpool John Moores University, Liverpool Science Park IC 2, 146 Brownlow Hill, UK
[27] Crimean Astrophysical Observatory RAS, P/O Nauchny, 298409, Crimea[†]
[28] Special Astrophysical Observatory, Russian Academy of Sciences, 369167, Nizhnii Arkhyz, Russia
[29] Pulkovo Observatory, St. Petersburg, 196140, Russia

[30] Institut de Radioastronomie Millimétrique, Avenida Divina Pastora, 7, Local 20, E-18012 Granada, Spain
[31] Max-Planck-Institut für Radioastronomie, Auf dem Hügel 69, D-53121 Bonn, Germany
[32] Center for Astrophysics—Harvard & Smithsonian, 60 Garden Street, Cambridge, MA 02138, USA
[33] Perkins Telescope Observatory, Boston University, 725 Commonwealth Avenue, Boston, MA 02215, USA
[34] Orchideenweg 8, 53123 Bonn, Germany
[35] Graduate School of Sciences, Tohoku University, Aoba-ku, 980-8578 Sendai, Japan
[36] Korea Astronomy and Space Science Institute, 776 Daedeok-daero, Yuseong-gu, Daejeon 34055, Republic of Korea
[37] University of Science and Technology, Korea, 217 Gajeong-ro, Yuseong-gu, Daejeon 34113, Republic of Korea
[38] Special Astrophysical Observatory of Russian Academy of Sciences, Nizhnij Arkhyz, Karachai-Cherkessian Republic, 369167, Russia
[39] Instituto de Estudios Astrofísicos, Facultad de Ingeniería y Ciencias, Universidad Diego Portales, Santiago, Región Metropolitana, 8370191, Chile
[40] INAF Osservatorio Astronomico di Cagliari, Via della Scienza 5, 09047 Selargius (CA), Italy
[41] Istituto Nazionale di Fisica Nucleare, Sezione di Pisa, Largo B. Pontecorvo 3, 56127 Pisa, Italy
[42] Dipartimento di Fisica, Universitá di Pisa, Largo B. Pontecorvo 3, 56127 Pisa, Italy
[43] Dipartimento di Matematica e Fisica, Universitá degli Studi Roma Tre, Via della Vasca Navale 84, 00146 Roma, Italy
[44] Istituto Nazionale di Fisica Nucleare, Sezione di Torino, Via Pietro Giuria 1, 10125 Torino, Italy
[45] Dipartimento di Fisica, Universitá degli Studi di Torino, Via Pietro Giuria 1, 10125 Torino, Italy
[46] INAF Osservatorio Astrofisico di Arcetri, Largo Enrico Fermi 5, 50125 Firenze, Italy
[47] Dipartimento di Fisica e Astronomia, Universitá degli Studi di Firenze, Via Sansone 1, 50019 Sesto Fiorentino (FI), Italy
[48] Istituto Nazionale di Fisica Nucleare, Sezione di Firenze, Via Sansone 1, 50019 Sesto Fiorentino (FI), Italy
[49] Science and Technology Institute, Universities Space Research Association, Huntsville, AL 35805, USA
[50] Istituto Nazionale di Fisica Nucleare, Sezione di Roma "Tor Vergata," Via della Ricerca Scientifica 1, 00133 Roma, Italy
[51] Department of Physics and Kavli Institute for Particle Astrophysics and Cosmology, Stanford University, Stanford, CA 94305, USA
[52] Institut für Astronomie und Astrophysik, Universität Tübingen, Sand 1, 72076 Tübingen, Germany
[53] Astronomical Institute of the Czech Academy of Sciences, Boční II 1401/1, 14100 Praha 4, Czech Republic
[54] RIKEN Cluster for Pioneering Research, 2-1 Hirosawa, Wako, Saitama 351-0198, Japan
[55] NASA Goddard Space Flight Center, Greenbelt, MD 20771, USA
[56] Yamagata University, 1-4-12 Kojirakawa-machi, Yamagata-shi 990-8560, Japan
[57] Osaka University, 1-1 Yamadaoka, Suita, Osaka 565-0871, Japan
[58] University of British Columbia, Vancouver, BC V6T 1Z4, Canada
[59] International Center for Hadron Astrophysics, Chiba University, Chiba 263-8522, Japan
[60] Department of Physics and Astronomy and Space Science Center, University of New Hampshire, Durham, NH 03824, USA
[61] Physics Department and McDonnell Center for the Space Sciences, Washington University in St. Louis, St. Louis, MO 63130, USA
[62] Istituto Nazionale di Fisica Nucleare, Sezione di Napoli, Strada Comunale Cinthia, 80126 Napoli, Italy
[63] Université de Strasbourg, CNRS, Observatoire Astronomique de Strasbourg, UMR 7550, 67000 Strasbourg, France
[64] Graduate School of Science, Division of Particle and Astrophysical Science, Nagoya University, Furo-cho, Chikusa-ku, Nagoya, Aichi 464-8602, Japan
[65] Department of Physics and Astronomy, Louisiana State University, Baton Rouge, LA 70803, USA
[66] Department of Physics, The University of Hong Kong, Pokfulam, Hong Kong
[67] Department of Astronomy and Astrophysics, Pennsylvania State University, University Park, PA 16802, USA
[68] Université Grenoble Alpes, CNRS, IPAG, 38000 Grenoble, France
[69] Dipartimento di Fisica e Astronomia, Universitá degli Studi di Padova, Via Marzolo 8, 35131 Padova, Italy
[70] Mullard Space Science Laboratory, University College London, Holmbury St Mary, Dorking, Surrey RH5 6NT, UK
[71] Anton Pannekoek Institute for Astronomy & GRAPPA, University of Amsterdam, Science Park 904, 1098 XH Amsterdam, The Netherlands
[72] Guangxi Key Laboratory for Relativistic Astrophysics, School of Physical Science and Technology, Guangxi University, Nanning 530004, People's Republic of China

Received 2024 October 23; revised 2025 March 21; accepted 2025 April 12; published 2025 June 20

Abstract

X-ray polarization is a unique new probe of the particle acceleration in astrophysical jets made possible through the Imaging X-ray Polarimetry Explorer. Here we report on the first dense X-ray polarization monitoring campaign on the blazar Mrk 421. Our observations were accompanied by an even denser radio and optical polarization campaign. We find significant short-timescale variability in both X-ray polarization degree and angle, including an $\sim 90^{\circ}$ angle rotation about the jet axis. We attribute this to random variations of the magnetic field, consistent with the presence of turbulence but also unlikely to be explained by turbulence alone. At the same time, the degree of lower-energy polarization is significantly lower and shows no more than mild variability. Our campaign provides further evidence for a scenario in which energy-stratified shock-acceleration of relativistic electrons, combined with a turbulent magnetic field, is responsible for optical to X-ray synchrotron emission in blazar jets.

Unified Astronomy Thesaurus concepts: Blazars (164); Jets (870); X-ray astronomy (1810); Shocks (2086); Markarian galaxies (1006); Time domain astronomy (2109); Polarimetry (1278); Radio jets (1347)

1. Introduction

Blazars are powerful active galactic nuclei (AGN) with relativistic jets emitting across the electromagnetic (and possibly high-energy particle) spectrum (e.g., R. Blandford et al. 2019; T. Hovatta & E. Lindfors 2019). Their extreme brightness and variability are attributed to relativistic effects dominating their multiwavelength emission due to orientation of the jets toward the line of sight (e.g., I. Liodakis et al. 2018). The broad spectral energy distribution (SED) of high-

† "While the AAS journals adhere to and respect UN resolutions regarding the designations of territories (available at http://www.un.org/press/en), it is our policy to use the affiliations provided by our authors on published articles."

Table 1
Summary of X-Ray Observations

Observatory	Obsid	Start Date	End Date
IXPE	02008199	2023-12-06 21:28:11.792	2023-12-22 07:44:27.400
NuSTAR	60902024002	2023-12-06 23:26:00	2023-12-07 10:31:09
NuSTAR	60902024004	2023-12-11 12:36:00	2023-12-12 00:11:09
NuSTAR	60902024006	2023-12-18 06:41:09	2023-12-18 18:16:09
NuSTAR	60902024008	2023-12-20 19:31:00	2023-12-21 06:41:09
XMM	0902112401	2023-12-07 00:16:39	2023-12-07 03:53:19
XMM	0902112501	2023-12-08 12:53:01	2023-12-08 18:16:21
XMM	0920900201	2023-12-11 12:52:35	2023-12-11 18:08:23
XMM	0920901301	2023-12-14 04:14:29	2023-12-14 10:54:29

synchrotron-peaked (HSP, $\nu_{\rm syn} > 10^{15}$ Hz) blazars is characterized by a synchrotron component extending from radio to X-rays, plus a high-energy component from X-rays to TeV γ-rays of currently debated origins.

Since its launch in December 2021, the Imaging X-ray Polarimetry Explorer (IXPE; M. C. Weisskopf et al. 2022) has been shaping our view of high-energy processes in the Universe, including jet–disk geometry as well as particle acceleration and emission in astrophysical jets from accreting black hole systems (e.g., H. Krawczynski et al. 2022; S. R. Ehlert et al. 2022; H. L. Marshall et al. 2024). The first IXPE observation of the blazar Mrk 501 measured a factor of $\sim$2 higher X-ray polarization than at optical or radio wavelengths, with the electric-vector position angles (EVPAs) at all sampled wavelengths roughly aligned with the jet axis on the sky (I. Liodakis et al. 2022), as measured with Very Long Baseline Array (VLBA) imaging (e.g., Z. R. Weaver et al. 2022). Synchrotron radiation with such an EVPA arises in a plasma with a mean magnetic field direction aligned perpendicular to the jet axis, as expected for a shock-compressed or helical (or toroidal) field. The observed degree of polarization was a factor of $\gtrsim$7 lower than the maximum value of 70%–75% and time-variable, both of which are characteristics of a turbulent magnetic field (A. P. Marscher 2014). The presence of a shock can explain how the radiating electrons are accelerated. Radiative energy losses as the electrons propagate away from the shock front lead to energy stratification that causes the emission region to be confined closer to the shock front at higher photon energies (A. P. Marscher & W. K. Gear 1985; A. P. Marscher 2014; E. Angelakis et al. 2016; F. Tavecchio et al. 2018). The emission regions at different frequencies are therefore, at most, only partially cospatial, with the larger, lower-frequency regions containing a greater number of cross-polarized turbulent cells, which causes their polarization to be lower. Subsequent IXPE observations of blazars Mrk 421 (L. Di Gesu et al. 2022), 1ES 1959+650 (M. Errando et al. 2024), 1ES 0229+200 (S. R. Ehlert et al. 2023), PG 1553+113 (R. Middei et al. 2023), and PKS 2155-304 (P. M. Kouch et al. 2024) provided further support for this emerging picture.

Arguably, the most interesting X-ray polarization behavior has been found in Mrk 421. While the first observation found a similar trend of X-ray higher polarization than that at longer wavelengths, as for Mrk 501, two subsequent observations revealed the first detection of an X-ray polarization angle rotation (L. Di Gesu et al. 2023). Rotations of the polarization angle are often detected at optical wavelengths (e.g., A. P. Marscher et al. 2008; D. Blinov et al. 2015, 2018; I. Liodakis et al. 2020), with long-term rotations associated with gamma-ray flaring (D. Blinov et al. 2021). But so far, no clear single cause has been identified. Further change in the X-ray polarization angle was detected in the fourth IXPE observation (D. E. Kim et al. 2024a), which is possibly associated with the ejection of a new moving radio knot found in contemporaneous VLBA images, although the connection between the X-ray rotation and radio ejection requires further investigation. This would, however, be in line with the optical polarization behavior of some blazars with lower synchrotron SED peaks ($\nu_{\rm syn} < 10^{14}$ Hz, A. P. Marscher et al. 2008, 2010; I. Liodakis et al. 2020) than those of Mrk 421 and Mrk 501, whose SEDs peak at X-ray energies, classifying them as HSP sources (e.g., M. Ajello et al. 2022).

Here we present the first dense X-ray polarization monitoring of a blazar, Mrk 421, with IXPE measurements carried out in four segments during 2023 December 6–22, the last blazar observations during IXPE's 2 yr prime mission. In Section 2 we describe our X-ray and multiwavelength observations, in Section 3 we present our results, and in Section 4 we discuss our findings.

2. Observations and Data Reduction

2.1. X-Rays

Mrk 421 was observed by IXPE in 2023 between December 6 and 22, as well as by NuSTAR and XMM-Newton over multiple epochs during this time period. The observations used in our analysis are listed in Table 1.

2.1.1. NuSTAR

NuSTAR observed Mrk 421 four times during the IXPE campaign, on 2023 December 6 for a net focal plane module A/B exposure time (respectively) of 21.29/21.13 ks[73] (ObsID: 60902024002), on 2023 December 11 for a net exposure time of 21.2/21.1 ks (ObsID: 60902024004), on 2023 December 18 for a net exposure time of 17.4/17.4 ks (ObsID: 60902024006), and on 2023 December 20 for a net exposure time of 20.6/20.4 ks ″(ObsID:60902024008). The NuSTAR spectra were extracted using a circular 1′ radius source region and a circular 100″ radius background region. The spectral extraction was accomplished with `HEASOFT` version 6.33, `NUSTARDAS` version 2.1.2, and CALDB version 20240229. Each spectrum was grouped to have a minimum of 30 counts per bin. Above 50 keV the background became stronger than the source, so we limit NuSTAR photon energies to 3.0–50.0 keV in spectral fits that incorporate NuSTAR data

[73] The focal plane module A & B (FPMA,FPMB respectively) exposure times are written as FPMA/FPMB.

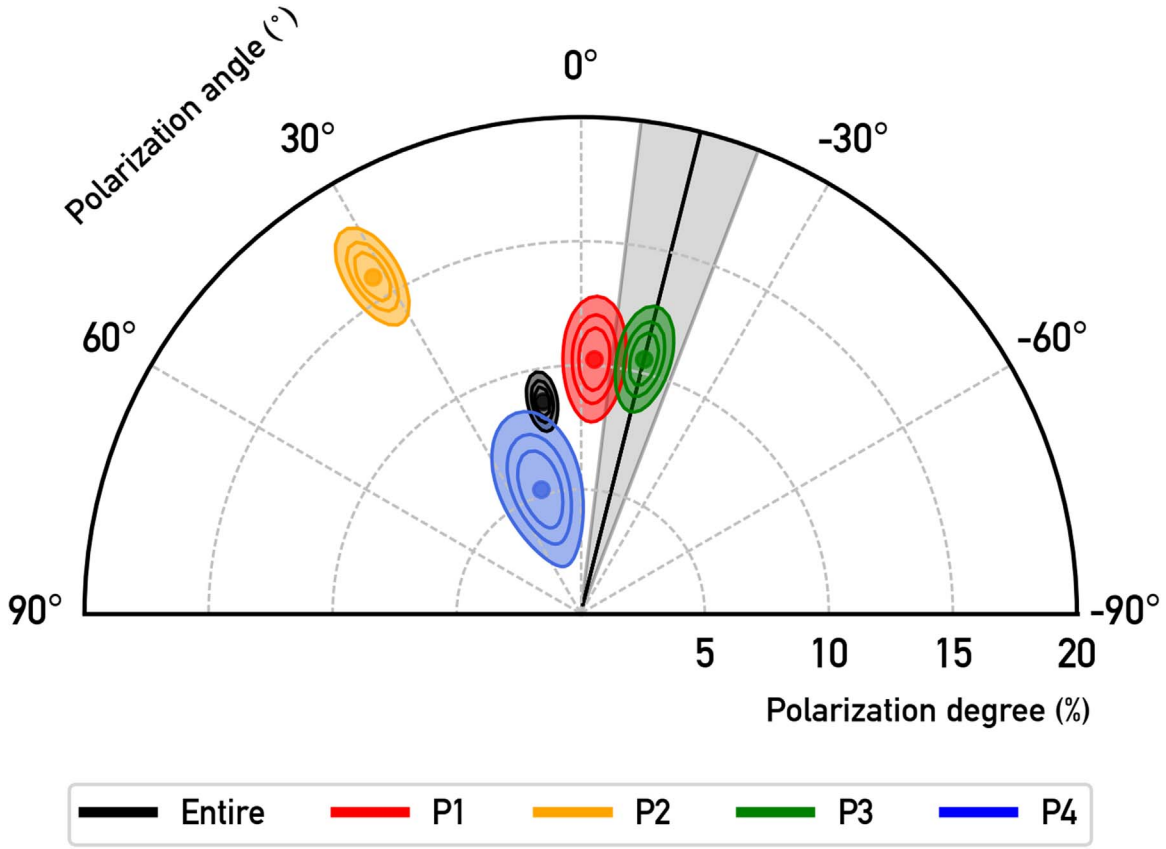

Figure 1. Time-averaged X-ray polarization contours for each of the four IXPE epochs for this campaign, labeled P1 (red), P2 (yellow), P3 (green), and P4 (blue), respectively, in order of time. "Entire" (black) represents all data for the campaign. Radial offset from the origin corresponds to polarization degree Π, and angle corresponds to polarization angle ψ. Contours are drawn at 68.27%, 90.00%, and 99.00% confidence levels, according to a χ^2 test with two degrees of freedom. The black line and gray shading in the unified plot represents the position angle of the jet on the sky in degrees, as observed by the VLBA at 43 GHz.

(see Section 2.1.3). The instrumental cross-normalization constant for FPMB was set to be 1.04 times the normalization constant for FPMA, as in K. K. Madsen et al. (2015).

2.1.2. XMM-Newton

XMM-Newton observed Mrk 421 four times during the IXPE campaign: on 2023 Dec 7 for a duration of 13.0 ks (Obsid: 0902112401), on 2023 December 8 for a duration of 19.4 ks (Obsid: 0902112501), on 2023 December 11 for an exposure time of 20.0 ks (Obsid: 0920900201), and on 2023 Dec 14 for an exposure time of 24.0 ks (Obsid: 092091301). All observations used the timing data mode and thick filter for the EPIC instrument. We reprocessed the observations using XMM SAS release 20230412_1735-21.0.0 and filtered the light curves for background flares.

MOS1 data were unavailable for analysis. We initially extracted spectra from the full timing window for both MOS2 and PN cameras using standard timing mode threads. To test for photon pile-up, we used the *epatplot* tool, and found a ∼20% excess of double events. We fit NuSTAR spectra to an absorbed power law and used `WebPIMMS`[74] to predict PN pile-up. The predicted PN count rate was well below pile-up thresholds and predicted pile-up rates were negligible. As a precaution against pile-up, we used only single events and excised the brightest "core" rows by iteratively masking them from the spectral extraction. We increased the size of the mask by one pixel in each direction per iteration, until the best fit to a simple absorbed power law produced negligible (< 1%) change in $n_{\rm H}$, power-law index, and normalization. Given the low expected pile-up, the actual goodness of the power-law model fit is irrelevant for determining the exclusion zone, only the variation in the model approximation in order to determine the row-specific impact of pile-up.

2.1.3. IXPE

IXPE observed Mrk 421 during four separate pointings from 2023 December 6 to 22, spanning 15.4 days (ObsID: 02008199). The pointings cover Mrk 421 for 927 ks, of which 514 ks is exposure (after accounting for factors such as Earth eclipses). The four observation periods are simultaneous with the four NuSTAR observations. Using the same methods as D. E. Kim et al. (2024a), we calculated the polarization angle and degree for each pointing. These are shown in Figure 1. The *I*, *Q*, and *U* spectra were extracted using `ixpeobssim` (L. Baldini et al. 2022) version 30.6.3, within a circular source region of 1′. The background was subtracted from an annular region with inner radius 2′ and outer radius 5′. The CALDB IRF version 13 (date 2023 July 2) in `ixpeobssim` was used for calibration. The spectra were weighted according to instrumental response. The *I* spectrum was grouped with a minimum of 30 counts/bin, while the *Q* and *U* spectra were grouped within equal 0.2 keV width bins. The polarization measurements were performed using the `pcube` algorithm (L. Baldini et al. 2022) and were background subtracted with a

[74] https://heasarc.gsfc.nasa.gov/cgi-bin/Tools/w3pimms/w3pimms.pl

Table 2
Results of spectropolarimetric fitting for the `constant*tbabs*polconst*zlogpar` model

	Int 1	Int 2	Int 3	Int 4
PD(%)	12 ± 2	19 ± 1	12 ± 1	6 ± 2
PA(°)[a]	−2.6 ± 3.9	32 ± 2.2	−14 ± 3.2	19 ± 9.7
α	2.8 ± 0.01	2.8 ± 0.01	2.9 ± 0.01	2.9 ± 0.01
β	0.170 ± 0.05	0.37 ± 0.02	0.23 ± 0.02	0.33 ± 0.02
Flux[b]	$1.85^{+0.01}_{-0.01}$	$2.27^{+0.03}_{-0.03}$	$2.90^{+0.01}_{-0.01}$	$2.64^{+0.03}_{-0.03}$
χ^2/d.o.f.	2122/1583	1416/1245	1355/1253	1438/1215

Notes. We note that the values for α and β are those from NuSTAR.
[a] Measured counterclockwise from west to east, −90° to +90°.
[b] The 2–8 keV observed flux in units of 10^{-10} erg cm^{-2} s^{-1}.

backscale ratio of 1/20. The spectra used in the spectropolarimetric fit were also background subtracted. The energy range 2.0–8.0 keV was used for the entire IXPE analysis.

Spectropolarimetric Fitting. For each IXPE observation, we jointly fit the *I*, *Q*, and *U* spectra together with the corresponding simultaneous NuSTAR and XMM-Newton observations.

We started with a `constant*tbabs*polconst* zlogpar` model, where `constant` is the instrumental cross-normalization constant, `tbabs` represents Galactic absorption, and `zlogpar` is a redshifted log-parabolic model similar to what has been used in the past to fit Mrk 421's X-ray spectrum (E. Massaro et al. 2004; L. Di Gesu et al. 2022). The spectral distribution is expressed in the form

$$N(E) = K(E(1+z)/E_p)^{(\alpha-\beta\log(E(1+z)/E_p))}. \quad (1)$$

In this equation, E_p is the pivot energy, α is the spectral slope at the pivot energy, and β is an indicator of spectral curvature at the peak. K is a normalization constant with units of photons/(cm^2 s keV). We fix the pivot energy to 5 keV (e.g., M. Baloković et al. 2016; L. Di Gesu et al. 2022; R. Middei et al. 2022). We attempted to add a `zphabs` model to take into account absorption at the source, but it did not improve the fit, so it was dropped. We therefore fit all four IXPE observations with a `constant*tbabs*polconst*zlogpar` model.

The results of the fits are tabulated in Table 2. The columns sort the results by the corresponding IXPE observation, while the rows represent the time-averaged PD, the time-averaged PA, α, β, the rest frame 2–10 keV flux, and the reduced χ^2 for each observation. The reduced χ^2 values of the fits range between 1.08 and 1.34, suggesting that while our model may be a reasonable first approximation, there is a need for additional model complexity. The XMM spectra in particular have notably strong residuals at some energies. The PD varies from 6 ± 2% to 20 ± 1% between observations, while the PA ranges from −14 ± 3° to +32 ± 2°. Comparable results have been found in A. M. Bharathan et al. (2024), averaging over the first 70 ks of the IXPE exposure. These spectra and fits are plotted in Appendix A.

Time Variability. We investigated polarization variability over time by applying the χ^2 test of the constant model on different timescales of binning over the entire observation period, following D. E. Kim et al. (2024a). This test examines the statistical significance of the variability by estimating the null hypothesis probability ($P_{\rm Null}$) of each constant model fitting on the normalized q and u Stokes parameters, while taking into account the uncertainty of each measurement. We divided the entire observation period into 10–35 subperiods, corresponding to ∼ 130 ks to ∼ 40 ks, respectively. As a result, we obtained less than 1% for the null hypothesis probability of the constant model for all cases of time binning of q and u Stokes parameters. The highest null hypothesis probability for q was 2.2×10^{-8}, which corresponds to an out-of-range value of ∼ 5.5σ (∼5.0σ for ⩾1 bin of 31), and we measured zero probability for the u Stokes parameter. Hence, we found evidence of statistically significant polarization variability over time from this observing period. Figure 2 shows the polarization measurements split in 31 bins (of size ∼43 ks per bin), which provided the largest number of statistically significant polarization variations.

In order to compare polarimetric variability with changes in the X-ray flux and spectral shape, we calculate the hard (H; 4–8 keV) and soft (S; 2–4 keV) fluxes, as well as a hardness ratio HR as a proxy for spectral shape, using the same ∼43 ks binning scheme as with time-resolved polarimetry. We define the hardness ratio HR = $(H - S)/(H + S)$, where H is the 4–8 keV flux and S is the 2–4 keV flux. The variation in these quantities is shown in Figure 3. We note a flare in both H and S by a factor of ∼2 at MJD ∼ 60299, after which the flux gradually decays over the next ≳10 days, with significant variability on ∼43 ks scales but remains elevated. The trend on timescales of days (most notably including the large flare) is broadly consistent with harder-when-brighter (as with L. Di Gesu et al. 2023). But there are obvious deviations from this trend on timescales of ∼8 hr. Another notable deviation is that the softest points (at MJD ∼ 60297) occur during this elevated, decaying state, after which the hardness (but not flux) becomes comparable to preflare conditions.

2.2. Optical Observations

Mrk 421 was observed by several telescopes in BVRI bands during all four segments of the IXPE observations. These facilities included the Kanata telescope using the Hiroshima Optical and Near-InfraRed camera (HONIR; K. S. Kawabata et al. 1999; H. Akitaya et al. 2014), the Liverpool Telescope using the Multicolour OPTimised Optical Polarimeter (MOPTOP; H. Jermak et al. 2016; M. Shrestha et al. 2020), the LX-200 telescope of St. Petersburg State University (V. M. Larionov et al. 2008), the Nordic Optical Telescope (ALFOSC, analysis described in T. Hovatta et al. 2016 and K. Nilsson et al. 2018), Boston University's 1.8 m Perkins Telescope (with the PRISM camera, S. G. Jorstad et al. 2010), the Sierra Nevada Observatory (DIPOL-1; J. Escudero & D. Morcuende 2023; J. Otero-Santos et al. 2024; J. Escudero Pedrosa et al. 2024), the Skinakas Observatory (RoboPol, A. N. Ramaprakash et al. 2019), and the T-60 telescope at the

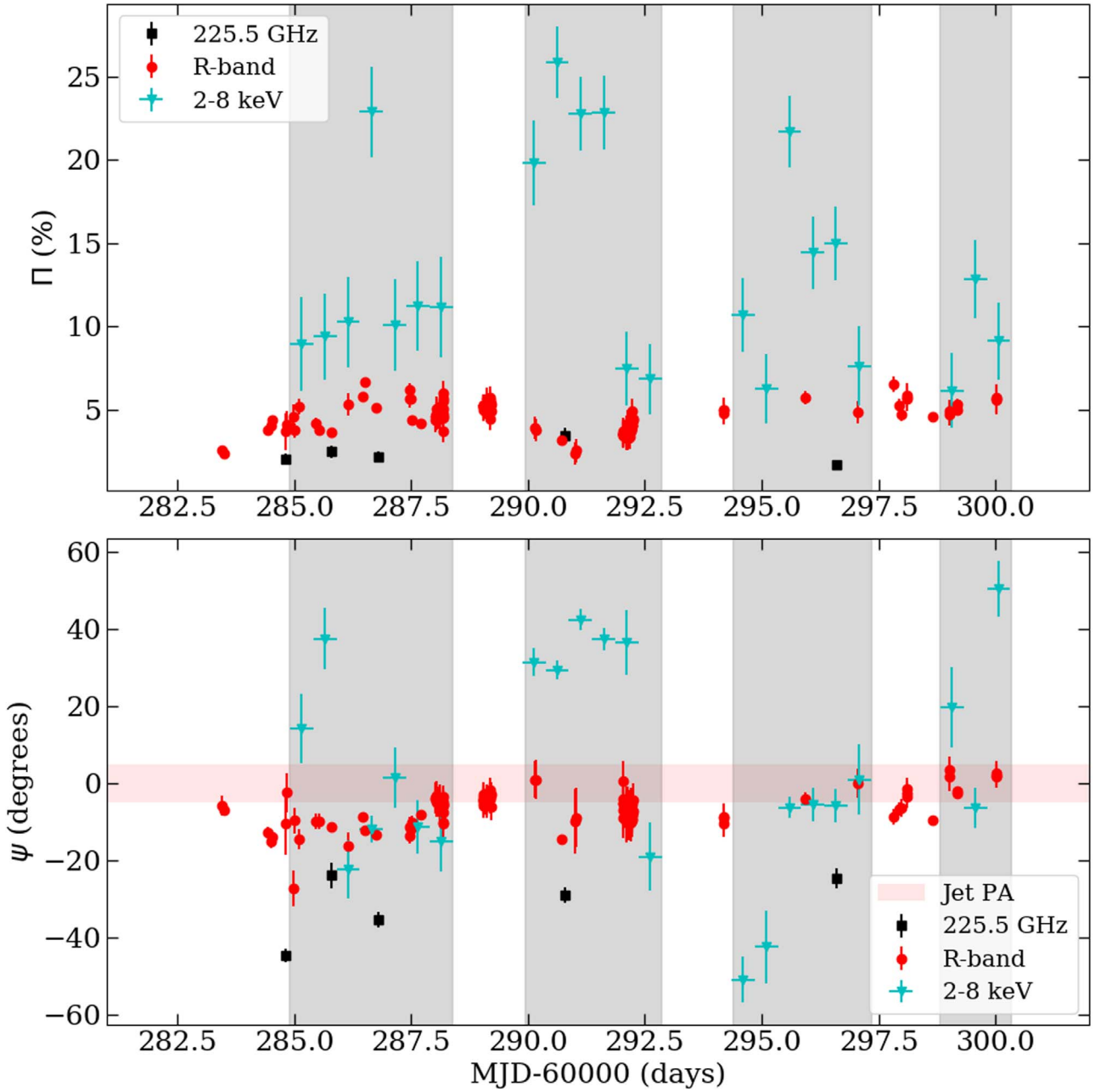

Figure 2. Time-resolved multiwavelength polarization observations. The top panel shows the polarization degree and the bottom panel shows the polarization angle, relative to the jet. The gray shaded areas in both panels mark the duration of the IXPE exposures, and the red shaded area in the bottom panel indicates the direction of the jet on the plane of the sky. We only show bins where the X-ray polarization degree is detected at the $>3\sigma$ level.

Haleakala observatory (V. Piirola 1973; A. V. Berdyugin et al. 2018; A. Berdyugin et al. 2019; V. Piirola et al. 2021). We corrected for dilution of the polarization by unpolarized host-galaxy light in the R-band by estimating the flux density of the host within a given aperture and subtracting from the total flux density following K. Nilsson et al. (2007) and T. Hovatta et al. (2016). Details of the data reduction and analysis of the different participating telescopes can be found in I. Liodakis et al. (2022), A. L. Peirson et al. (2023), and P. M. Kouch et al. (2024). The optical flux and polarization measurements are shown along with the IXPE results in Appendix B. The points labeled as *R*-band with a "†" correspond to *R*-band observations that we were unable to correct for the host-galaxy contribution, but are provided here for relative comparison.

2.3. Radio Observations

Radio observations covered frequencies from 4.8 to 225.5 GHz using the Effelsberg 100 m radio telescope (A. Kraus et al. 2003), the Korean VLBI Network (KVN), and the Submillimeter Array (SMA) polarimeter (D. P. Marrone & R. Rao 2008). The Effelsberg 4.8 and 14.2 GHz observations are part of the program Monitoring the Stokes *Q*, *U*, *I*, and *V* Emission of AGN jets in Radio (QUIVER, I. Myserlis et al. 2018). The KVN provided 25 GHz observations using the Yonsei and Tamna antennas in single-dish mode (S. Kang et al. 2015), and the SMA observations were performed as part of the SMA Monitoring of AGNs with POLarization (SMAPOL, I. Myserlis et al. 2024, in preparation) program at 225.5 GHz. Data from all radio observations are shown in Appendix B.

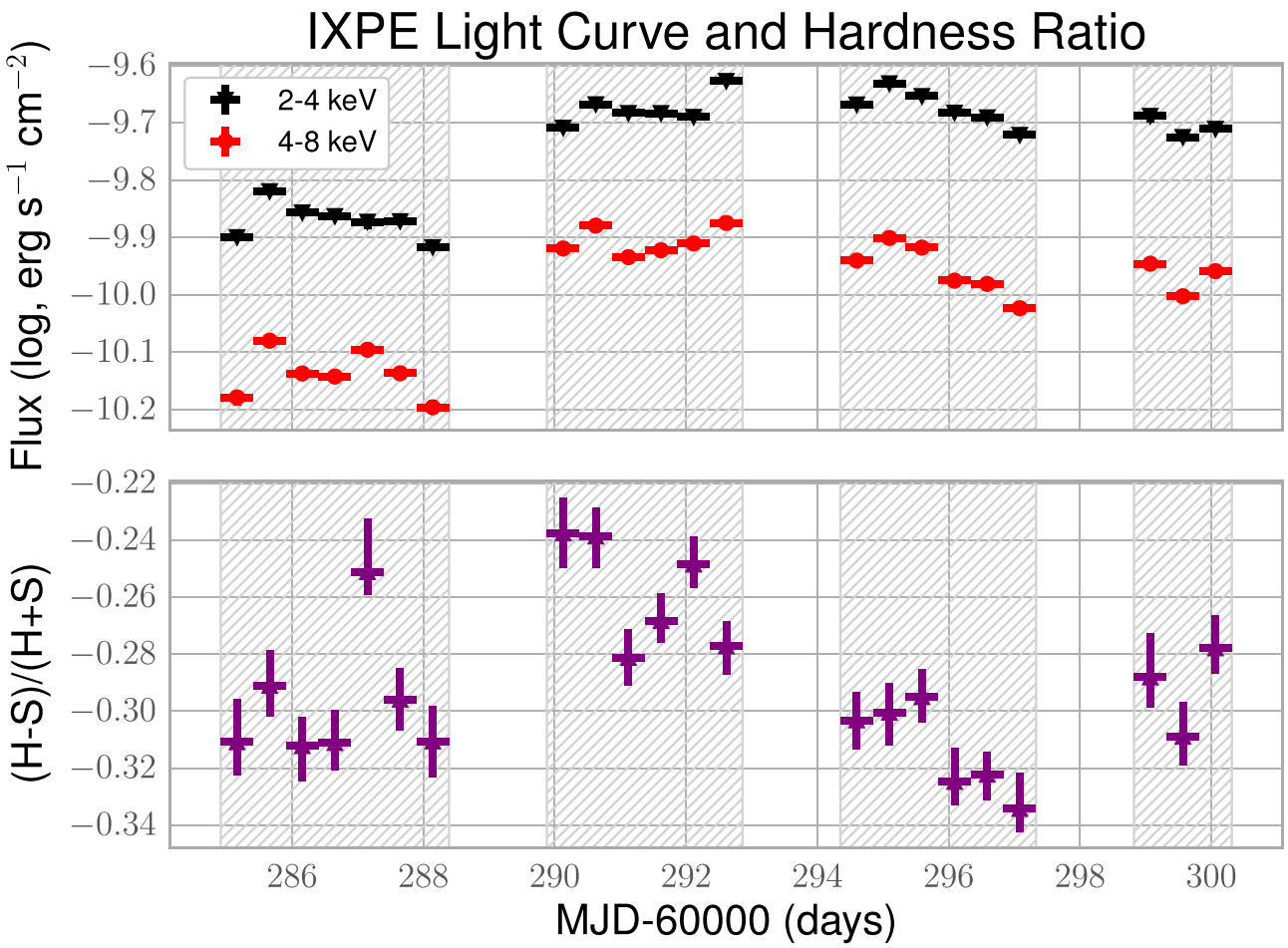

Figure 3. Top: light curves of the $\log_{10}$ IXPE flux for soft (2–4 keV, black triangles) and hard (4–8 keV, red dots) bands. Bottom: hardness ratios calculated from the soft and hard flux.

In the beginning of the second IXPE pointing, 2023 December 12 (RJD = 289, where RJD = JD−2460000.0), we obtained total and polarized intensity images of Mrk 421 with the Very Long Baseline Array (VLBA) at 43 GHz under the Boston University BEAM-ME project.[75] The data reduction was performed using the Astronomical Image Process System (AIPS) and Difmap software packages, as described in S. G. Jorstad et al. (2017). Figure 4 displays the total intensity image with the polarized intensity superposed, along with line segments indicating the EVPA. We have modeled the total intensity image by components with circular Gaussian brightness distributions. We measured the Stokes Q and U flux densities of these components (knots) and derived their PD and EVPA at 43 GHz. Table 3 lists the total intensity and polarization parameters of the three brightest components ($A0$, $J1$, and $J2$). This model fits the uv data very well, with a reduced χ^2 of 0.86. The location and size of each component is marked in Figure 4 by green circles. Knot A0, located at the southern end of the jet, represents the VLBI core of the jet, while the jet component nearest to the core, J2, defines the innermost jet direction as $\mathrm{PA_{jet}} = 1° \pm 5°$. This is, within the uncertainties, parallel to the parsec-scale jet direction of Mrk 421, $\mathrm{PA_{jet}} = -14° \pm 14°$, estimated based on 92 epochs of observations from 2007 to 2018 (Z. R. Weaver et al. 2022).

[75] www.bu.edu/blazars/BEAM-ME.html

3. Results

To probe short-term variability, we divide the IXPE observations into 31 bins as discussed above. Figure 2 shows the significantly detected X-ray polarization bins. Only one bin does not have a significant detection. We find rapid variability in both the polarization degree and angle. Between the second and third observations we also detect a significant rotation of the polarization angle by ∼90°. This is significantly less than the previously detected rotation in Mrk 421 of about 400° (L. Di Gesu et al. 2023). The direction of the polarization vector seems to vary about the jet axis, which is typically of HSP blazars (A. P. Marscher & S. G. Jorstad 2021, C.-T. J. Chen et al. 2024, L. Lisalda et al. 2025, submitted). We discuss the origin of the rotation below.

On the other hand, at radio wavelengths the degree of polarization of Mrk 421 is low (1%–3%), with a median of ∼2%. In the past, the millimeter-radio polarization angle has been fairly stable along $-29° \pm 8°$, consistent with the jet axis on the sky over long timescales, $-14° \pm 14°$ (see above). However, the direction of both the jet and the EVPA at 43 GHz in the innermost regions was $1° \pm 5°$ on 2023 December 12 (MJD = 60290) during the IXPE campaign (see Figure 4), identical with the optical EVPA. The EVPA of SMAPOL and QUIVER data exhibits a relatively stable frequency dependence across centimeter and millimeter wavelengths, suggestive of a Faraday screen with rotation measure RM $\sim -250\,\mathrm{rad/m^2}$ (R. N. Manchester 1972).

Table 3
Parameters of Jet Components at 43 GHz

Knot (1)	S,mJy (2)	R,mas (3)	PA_{jet},deg (4)	Size,mas (5)	$PD_{43\ GHz}$,% (6)	$EVPA_{43\ GHz}$,deg (7)
A0	335±15	0.0	⋯	0.05±0.02	3.0±0.4	2±4
J2	37±8	0.21±0.05	1±5	0.17±0.03	7.0±1.5	−25 ± 6
J1	25±10	0.52±0.09	−38 ± 7	0.4 7±0.10	18.0±7.5	−12 ± 10

Notes. Column identification: (1) name of component; (2) flux density, S, millijanskys; (3) distance from the core, R, milliarcseconds (mas); (4) position angle of the knot with respect to the core, PA_{jet}, degrees; (5) FWHM size of the component, mas; (6) degree of polarization, percentage; (7) position angle of polarization, degrees. All uncertainties are 1σ.

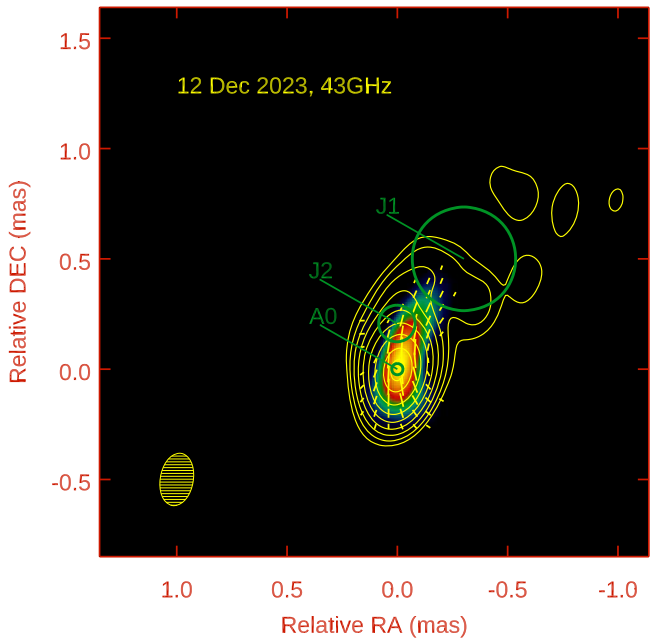

Figure 4. Total (contours) and polarized (color scale) intensity images of Mrk 421 at 43 GHz, convolved with an elliptical Gaussian beam of dimensions 0.24×0.15 mas^2 with major axis along PA $= -10°$. The global total intensity peak is 321 mJy beam^{-1} and the global polarized intensity peak is 9.6 mJy beam^{-1}. Yellow line segments within the image indicate the direction of polarization, while the length of each segment is proportional to the polarized intensity. Green circles designate the core, A0, and jet components, J1 and J2, according to model fitting to the uv data.

We find a similar behavior at optical wavelengths: there are no large variations in either flux, polarization degree, or polarization angle. The polarization degree smoothly changes from 2% to 6% with a median of about 4.5%. The polarization angle is roughly stable and along −7°, a bit offset from the jet axis. Compared to previous observations contemporaneous with IXPE, the source maintains consistent behavior at radio and optical wavelengths (D. E. Kim et al. 2024a).

The 31-bin light curve of the IXPE soft and hard flux is matched to the polarimetric binning and within any given epoch is consistent with increased spectral hardness at high flux, with the exception of epoch 2 (290 < MJD −60000 < 293), where there is no obvious correlation over a timescale of ∼days. After the first epoch (284 < MJD −60000 < 289), the flux increases by a factor of ∼2 and remains comparably high for the remainder of the campaign. This flare corresponds to an increase in hardness, $\sim 6\sigma$ above the mean value for the IXPE campaign (HR ∼ 0.295), as well as an increase in polarization degree from ∼10% to ∼25%, which is sustained over ∼2 days. The most extreme deviations of polarization angle from the jet value seem to be associated with either very hard (MJD −60000 ∼ 290) or very soft (MJD −60000 ∼ 296) spectra. Epochs 2 (290 < MJD −60000 < 293) and 3 (294 < MJD −60000 < 298) show a trend of decreasing HR, to below preflare levels, and the ∼90° rotation in X-ray polarization angle occurs during this trend, such that the softest HR values are associated with a return to the jet angle, a moderate degree of polarization (∼7%–15%), and rapid variability (≲day) of the polarization degree.

4. Discussion and Conclusions

We have presented the first dense monitoring of the X-ray polarization of a blazar with IXPE. We find large variations in the polarization degree and a rotation in the polarization angle. The origin of these rotations requires us to consider models varying from shocks moving along a helical magnetic field down the jet (A. P. Marscher et al. 2008), bent jets (A. A. Abdo et al. 2010), turbulence (A. P. Marscher 2014), shock–shock interactions (I. Liodakis et al. 2020), kink instabilities (H. Zhang et al. 2017), and magnetic reconnection (D. N. Hosking & L. Sironi 2020; H. Zhang et al. 2020), among others. S. Kiehlmann et al. (2017) concluded that relatively small (∼90°) rotations are likely to result from random walks of the magnetic field due to turbulence or emission originating in multiple zones. They also found that larger (>180°) rotations are often associated with γ-ray activity (A. P. Marscher et al. 2010; D. Blinov et al. 2015, 2018), particularly for long-term optical rotation (D. Blinov et al. 2021).

We test the random-walk scenario following S. Kiehlmann et al. (2017) and S. Kiehlmann et al. (2021), in a similar manner as in our previous analysis of the X-ray EVPA rotation detected in Mrk 421 (L. Di Gesu et al. 2023). We generate a large number of simulated polarization light curves by exploring the parameter space of number of cells and number of cells that change per day ($N_{\rm cell}$, $N_{\rm V\ ar}$, respectively). We then identify the simulations that produce similar polarization properties as those observed.

We apply the test to both the entire IXPE data set as well as to only the period of rotation between the second and third observational segments. For the former case, we use the median and interquantile range of the polarization degree and the interquantile range of the polarization angle. We require that the simulations produce values within 10% of those observed for the individual quantities. We are able to achieve a >50% success rate between simulations and observations, with the median polarization degree succeeding at a higher rate than the interquantile range of the polarization angle. However, when we require all conditions to be satisfied at the same time, the maximum success rate is only 1%. This is because the observed

quantities are better reproduced from different regions of the $N_{\rm cell}$, $N_{\rm V\ ar}$ parameter space, with little overlap. This is consistent with the findings of the larger statistical study of the optical RoboPol sample (S. Kiehlmann et al. 2017). For segments 2–3, we again require that the median and interquantile range of the polarization degree for the simulations be within 10% of that observed and that the simulations produce a rotation of the polarization angle that has an equal or larger amplitude. Figures showing the success rate of the simulations for the $N_{\rm cell}$, $N_{\rm V\ ar}$ parameter space are presented in Appendix C. For the polarization degree, we find similar results as in the entire data set. For the polarization angle, we find that more than 80% of the simulations are able to produce a rotation that has an amplitude that is equal to, or larger than, the observed value. However, similar to the entire data set, when we demand that all conditions are met, we can only achieve a success rate of ∼2%. Based on both tests, we conclude that a simple, pure random-walk model has only a low probability to reproduce the observed behavior.

Although at least some level of turbulence appears to be present, evident by the lower than theoretically expected polarization degree (see below), turbulence is unlikely to be the primary cause of the EVPA rotation. The observed behavior is likely more akin to a scenario where turbulent plasma passes through a more ordered magnetic field region, such as a shock (A. P. Marscher 2014).

During the period of the highly variable X-ray polarization ($\Delta\Pi > 10\%$), the radio and optical polarization is at most mildly variable ($\Delta\Pi < 4.5\%$ for R-band, $<2.5\%$ for all radio bands observed). The X-ray polarization degree reaches a maximum of 25%, 8× higher than the simultaneous optical polarization. Throughout our campaign, the X-rays remain consistently more polarized than the radio and optical emission, although there are time bins within which the ratio of X-ray to optical polarization is close to unity (such as MJD $-60000 \sim$ [292.5, 295.0, 297.0, 299.0], all of which occupy local X-ray flux maxima within the elevated flux after MJD $-60000 \sim 290$, except MJD $-60000 \sim 297.0$ which is at a local flux minimum). This, along with the time variability of the polarization, suggests that even in the X-ray emission region there is a significant turbulent component. The large deviation from the jet axis could occur if a new jet component is ejected from the core. In such a case, shock–shock interactions could induce turbulence that depolarizes the emission. Alternately, if the new component is differently polarized from the core, the overall polarization can cause a change in EVPA from the jet axis and a net drop in polarization (see, e.g., P. M. Kouch et al. 2025, for similar behavior). A new shock is not strictly necessary, though; a blob of electrons crossing the standing shock might also cause such behavior.

In general, a role for turbulence is suggested by the fact that we see only 25% polarization, compared to ∼70%–75% expected for synchrotron radiation in a perfectly ordered magnetic field. Some steady jet models would permit such a low polarization (e.g., F. Bolis et al. 2024), but would not explain the erratic variability.

Also in general, the most extreme variability of the X-ray polarization degree during this campaign is observed to occur on shorter timescales (∼12–48 hr over the entire campaign) than for the most extreme flux variability. The flare beginning MJD $-60000 \sim 290$ is associated with some of the strongest sustained X-ray polarization observed in Mrk 421 (typically $\lesssim$15%; L. Di Gesu et al. 2022, L. Di Gesu et al. 2023, D. E. Kim et al. 2024a), and afterwards the X-ray flux evolves little within a ±12% range over >10 days. Given that this large PD coincides with the beginning of the X-ray rotation, it is likely that the high degree of polarization is due to shock compression as the moving feature/blob crosses the standing core. That momentarily increases the polarization degree followed by a rapid drop and EVPA rotation as has been observed in low-peaked blazars in the optical. Such a scenario is expected to be analogous to high-peaked sources in X-ray polarization (I. Liodakis et al. 2020).

In comparison to flux variability, polarization variability timescales are shorter by a factor of >5 and possibly much more. This is due in part to the vector nature of polarization: for example, $N_{\rm cell}$ regions of equal flux but randomly directed polarizations could maintain a steady total flux, while the polarization degree varies about a mean value of $\langle\Pi\rangle \sim 75 N_{\rm cell}^{-1/2}\%$ with a standard deviation of $0.5\langle\Pi\rangle$ (A. P. Marscher & S. G. Jorstad 2021). The polarized emission could also occupy a region that subtends only a fraction of the X-ray emitting region. The 90° rotation occurs over an intermediate timescale (∼5 days). Harder-when-brighter behavior has previously been observed during 2022 June IXPE observations of polarization angle rotation in Mrk 421. This is consistent with shock acceleration, which may explain increased polarization in such a case (L. Di Gesu et al. 2023).

The maximum departure of the EVPA from the jet axis is observed between ∼2 and ∼5 days after the flare beginning no later than ∼MJD ∼ 60290.0, during a period of relatively slow flux decay that also coincides with a trend of spectral softening. The hardening of the spectrum during the flare maximum and softening thereafter are consistent with shock acceleration. This fits well the interpretation that shock compression leads to high PD, particle acceleration and hardening of the spectrum, followed by the rapid change of the EVPA, depolarization, and the eventual electron cooling that will soften the spectrum.

The significantly higher polarization and variability strongly points to the X-ray emission originating in a smaller region closer to the acceleration site, where the magnetic field is less disordered, than is the case for lower frequencies. Variations of the polarization angle about the jet axis give further evidence for particle acceleration in shocks (I. Liodakis et al. 2022). The evidence therefore supports the persistent emerging picture of energy-stratified shock acceleration in the jets of HSP blazars (e.g., D. E. Kim et al. 2024b).

Acknowledgments

The Imaging X-ray Polarimetry Explorer (IXPE) is a joint US and Italian mission. The US contribution is supported by the National Aeronautics and Space Administration (NASA) and led and managed by its Marshall Space Flight Center (MSFC), with industry partner Ball Aerospace (now, BAE Systems). The Italian contribution is supported by the Italian Space Agency (Agenzia Spaziale Italiana, ASI) through contract ASI-OHBI-2022-13-I.0, agreements ASI-INAF-2022-19-HH.0 and ASI-INFN-2017.13-H0, and its Space Science Data Center (SSDC) with agreements ASI-INAF-2022-14-HH.0 and ASI-INFN 2021-43-HH.0, and by the Istituto Nazionale di Astrofisica (INAF) and the Istituto Nazionale di Fisica Nucleare (INFN) in Italy. This research used data products provided by the IXPE Team (MSFC, SSDC, INAF, and INFN) and distributed with additional software tools by the

High-Energy Astrophysics Science Archive Research Center (HEASARC), at NASA Goddard Space Flight Center (GSFC).

I.L. was supported by the NASA Postdoctoral Program at the Marshall Space Flight Center, administered by Oak Ridge Associated Universities under contract with NASA. The IAA-CSIC coauthors acknowledge financial support from the Spanish "Ministerio de Ciencia e Innovación" (MCIN/AEI/10.13039/501100011033) through the Center of Excellence Severo Ochoa award for the Instituto de Astrofísica de Andalucía-CSIC (CEX2021-001131-S), and through grants PID2019-107847RB-C44 and PID2022-139117NB-C44. The Submillimeter Array is a joint project between the Smithsonian Astrophysical Observatory and the Academia Sinica Institute of Astronomy and Astrophysics and is funded by the Smithsonian Institution and the Academia Sinica. Maunakea, the location of the SMA, is a culturally important site for the indigenous Hawaiian people; we are privileged to study the cosmos from its summit. E.L. was supported by Academy of Finland projects 317636 and 320045.

The research at Boston University was supported in part by National Science Foundation grant AST-2108622, NASA Fermi Guest Investigator grant 80NSSC23K1507, NASA NuSTAR Guest Investigator grant 80NSSC24K0565, and NASA Swift Guest Investigator grant 80NSSC23K1145. The Perkins Telescope Observatory, located in Flagstaff, AZ, USA, is owned and operated by Boston University. This work was supported by NSF grant AST-2109127. We acknowledge the use of public data from the Swift data archive. Based on observations obtained with XMM-Newton, an ESA science mission with instruments and contributions directly funded by ESA Member States and NASA. Partly based on observations with the 100 m telescope of the MPIfR (Max-Planck-Institut für Radioastronomie) at Effelsberg.

Observations with the 100 m radio telescope at Effelsberg have received funding from the European Union's Horizon 2020 research and innovation program under grant agreement No. 101004719 (ORP). S.K., S.-S.L., W.Y.C., S.-H.K., and H.-W.J. were supported by the National Research Foundation of Korea (NRF) grant funded by the Korea government (MIST) (2020R1A2C2009003). The KVN is a facility operated by the Korea Astronomy and Space Science Institute. The KVN operations are supported by KREONET (Korea Research Environment Open NETwork), which is managed and operated by Korea Institute of Science and Technology Information (KISTI).

This work was supported by JST, the establishment of university fellowships toward the creation of science technology innovation, grant No. JPMJFS2129. This work was supported by Japan Society for the Promotion of Science (JSPS) KAKENHI grant No. JP21H01137. This work was also partially supported by Optical and Near-Infrared Astronomy Inter-University Cooperation Program from the Ministry of Education, Culture, Sports, Science and Technology (MEXT) of Japan. We are grateful to the observation and operating members of Kanata Telescope. The Liverpool Telescope is operated on the island of La Palma by Liverpool John Moores University in the Spanish Observatorio del Roque de los Muchachos of the Instituto de Astrofisica de Canarias with financial support from the UKRI Science and Technology Facilities Council (STFC) (ST/T00147X/1). B.A.-G., S.K., and I.L. were funded by the European Union ERC-2022-STG —BOOTES—101076343. The VLBA is an instrument of the National Radio Astronomy Observatory. The National Radio Astronomy Observatory is a facility of the National Science Foundation operated by Associated Universities, Inc.

Views and opinions expressed are, however, those of the author(s) only and do not necessarily reflect those of the European Union or the European Research Council Executive Agency. Neither the European Union nor the granting authority can be held responsible for them. This research has made use of data from the RoboPol program, a collaboration between Caltech, the University of Crete, IA-FORTH, IUCAA, the MPIfR, and the Nicolaus Copernicus University, which was conducted at Skinakas Observatory in Crete, Greece. D.B. acknowledges support from the European Research Council (ERC) under the Horizon ERC Grants 2021 program under the grant agreement No. 101040021.

The data in this study include observations made with the Nordic Optical Telescope, owned in collaboration by the University of Turku and Aarhus University, and operated jointly by Aarhus University, the University of Turku and the University of Oslo, representing Denmark, Finland, and Norway, the University of Iceland and Stockholm University at the Observatorio del Roque de los Muchachos, La Palma, Spain, of the Instituto de Astrofisica de Canarias. The data presented here were obtained in part with ALFOSC, which is provided by the Instituto de Astrofísica de Andalucía (IAA) under a joint agreement with the University of Copenhagen and NOT. We acknowledge funding to support our NOT observations from the Finnish Centre for Astronomy with ESO (FINCA), University of Turku, Finland (Academy of Finland grant nr 306531).

We thank the anonymous referee for many helpful comments and recommendations made that improved the quality of the paper.

Facilities: Effelsberg, IXPE, Kanata, KVN, Liverpool:2m, LX-200, NOT, NuSTAR, Perkins telescope, Swift, Skinakas:1.3m, SMA, OSN:0.9m, TU:0.6m.

Software: XSPEC (K. A. Arnaud 1996).

Appendix A
Spectropolarimetric Fit

Here we present figures showing the X-ray spectra from IXPE, XMM-Newton, and NuSTAR, as well as best-fit log-parabolic models. The first and second IXPE observations are shown in Figure 5, and third and fourth IXPE observations in Figure 6.

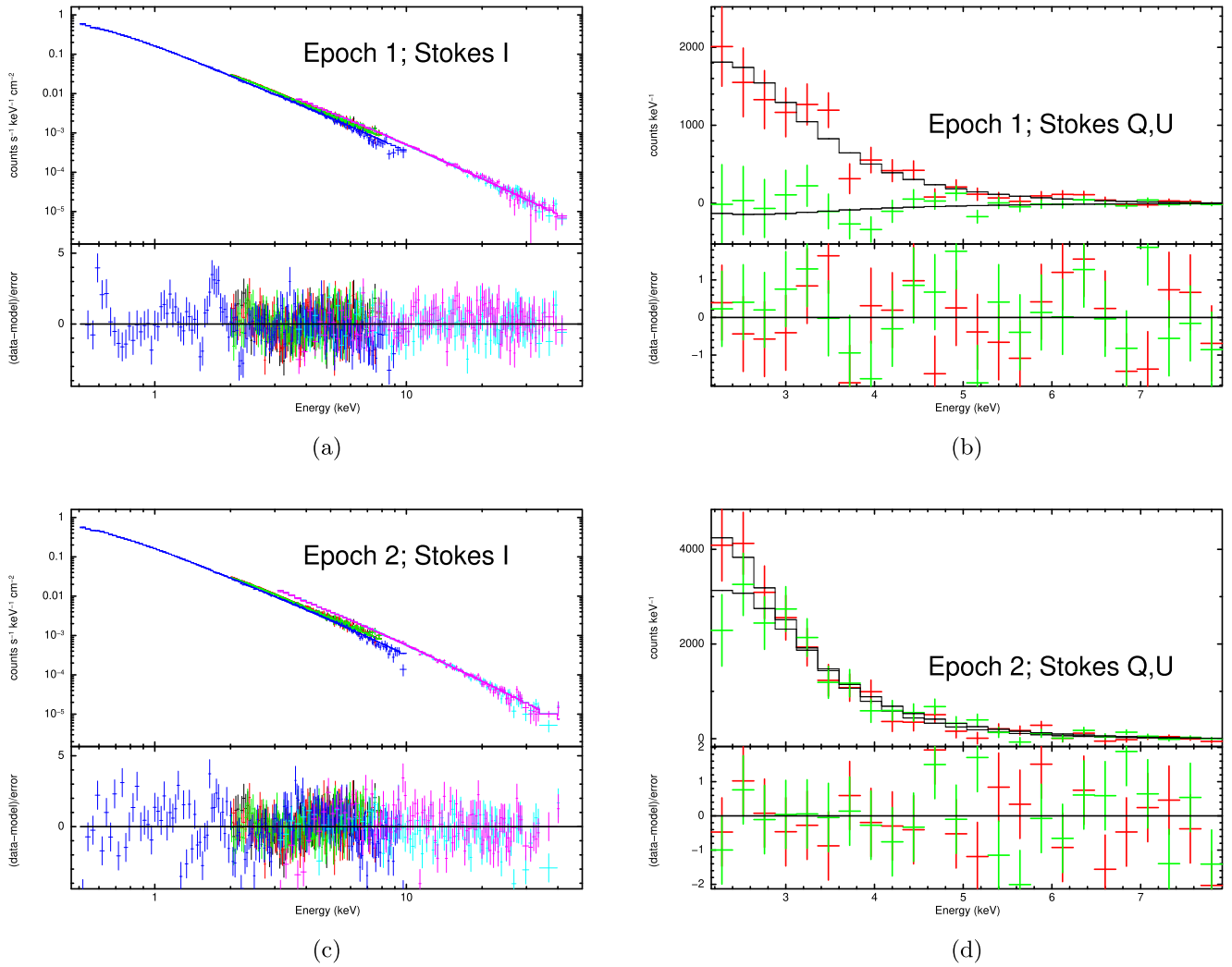

Figure 5. Unfolded I spectra (left) and Q and U spectra (right) for the first (a and b) and second (c and d) IXPE observations. In the unfolded spectra, dark blue is XMM, green, red, and black are IXPE, and pink and light blue are NuSTAR. In the Q and U spectra, red is Q and green is U. Data points are shown as error bars, the model is shown as a solid black step curve.

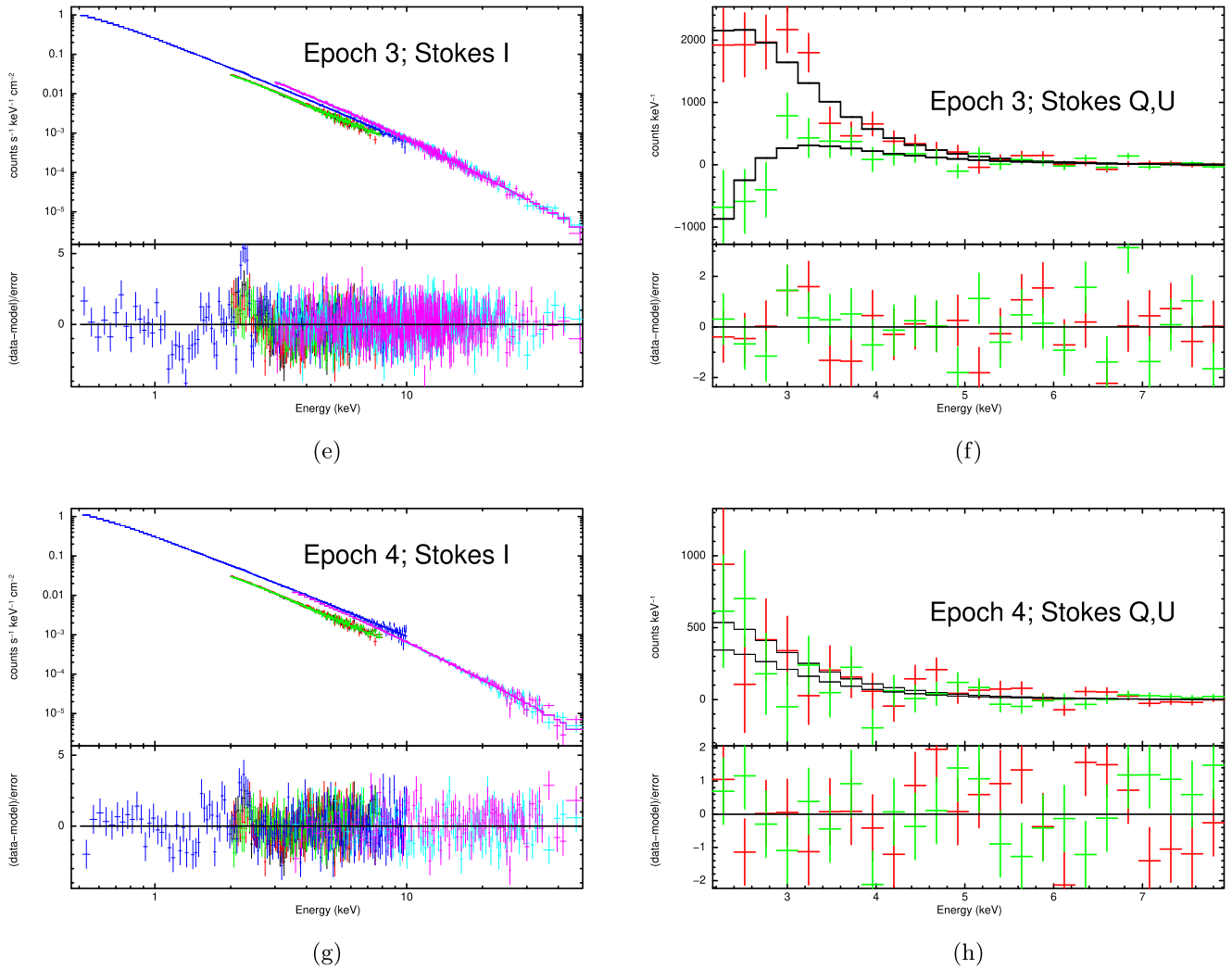

Figure 6. Unfolded I spectra (left) and Q and U spectra (right) for the third (e and f) and fourth (g and h) IXPE observations. In the unfolded spectra, dark blue is XMM, green, red, and black are IXPE, and pink and light blue are NuSTAR. In the Q and U spectra, red is Q and green is U. Data points are shown as error bars, the model is shown as a solid line.

Appendix B
Multiwavelength Polarization Observations

Here we present Figures 7 and 8, which show the flux density or magnitude of radio and optical observations (respectively) in comparison with the per-epoch time-averaged polarization degree and angle IXPE data for this campaign.

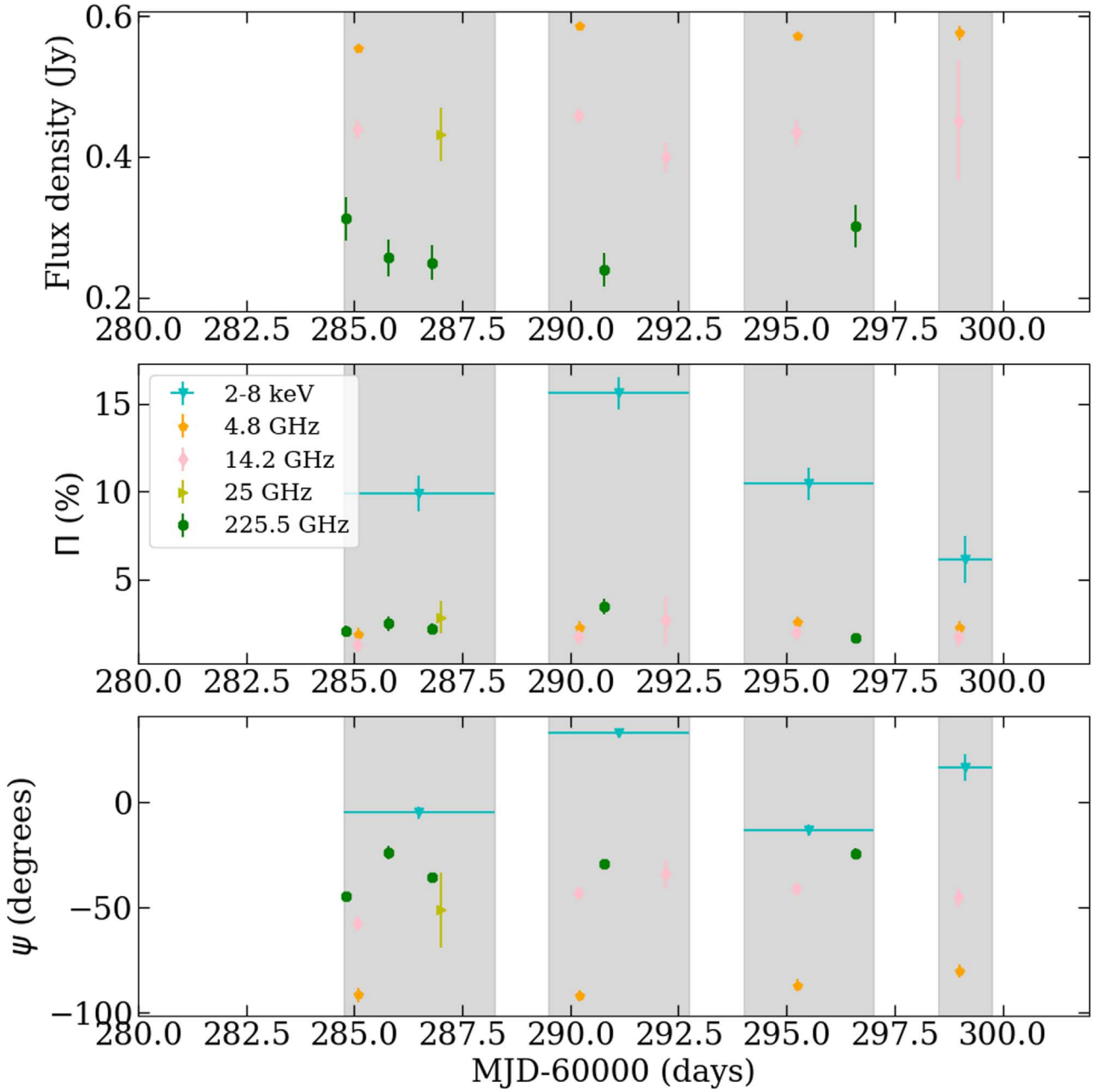

Figure 7. Integrated IXPE and simultaneous radio polarization observations of Mrk 421. The panels show flux density in Janskys (top), polarization degree in % (middle), and polarization angle in degrees (bottom). The gray shaded areas mark the duration of the IXPE observations. The symbols and colors for the different bands are marked in the legend and are the same for all panels.

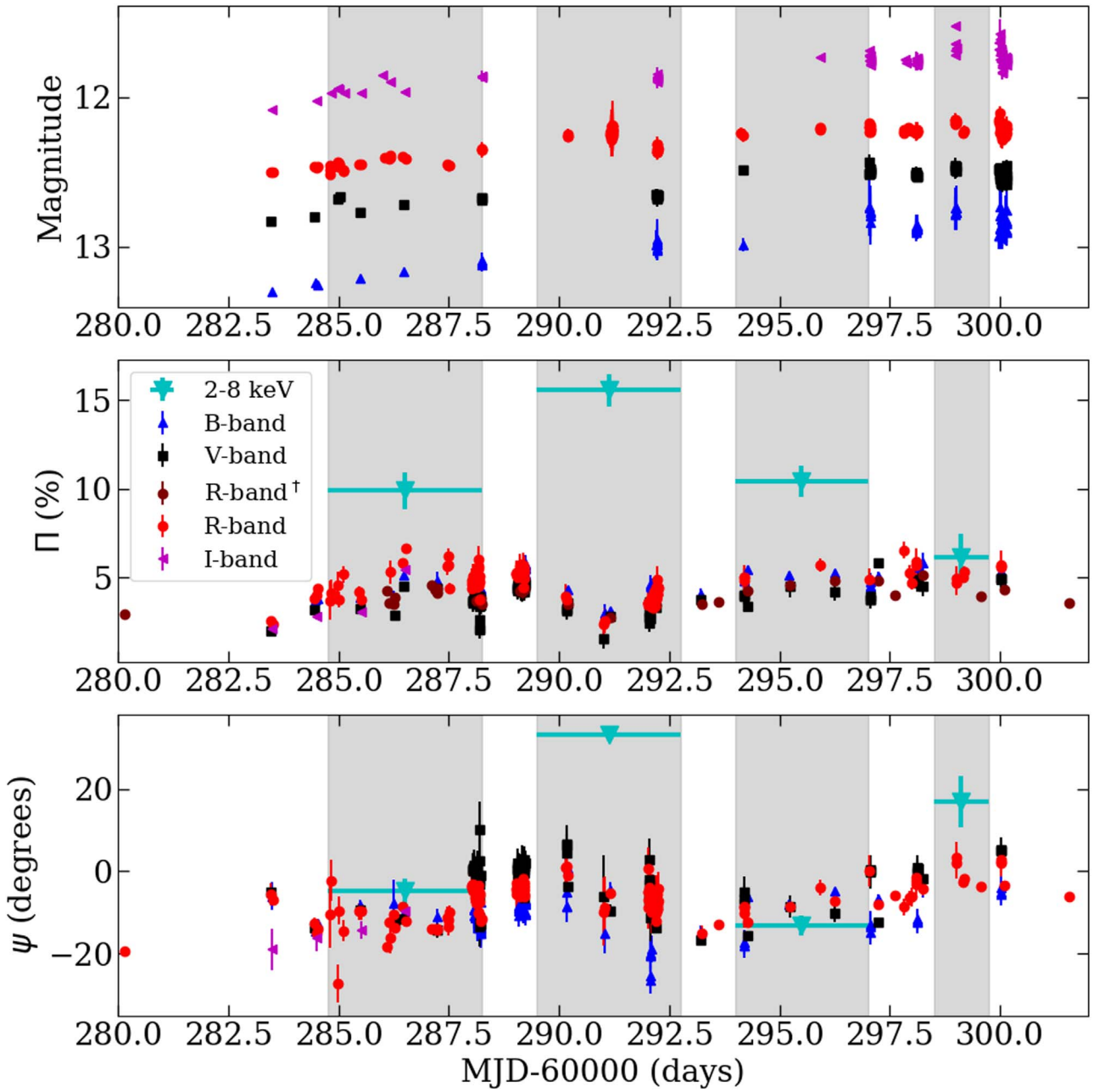

Figure 8. Integrated IXPE and simultaneous optical polarization observations of Mrk 421. The panels show brightness in magnitudes (top), polarization degree in % (middle), and polarization angle in degrees (bottom). The gray shaded areas mark the duration of the IXPE observations. The symbols and colors for the different bands are marked in the legend and are the same for all panels. † refers to *R*-band polarization degree that is uncorrected for host-galaxy dilution.

Appendix C
Random-walk Simulations

Here we present Figures 9, 10, 11, and 12, which show the success rate of the simulations for the $N_{\rm cell}$, $N_{\rm V\ ar}$ parameter space.

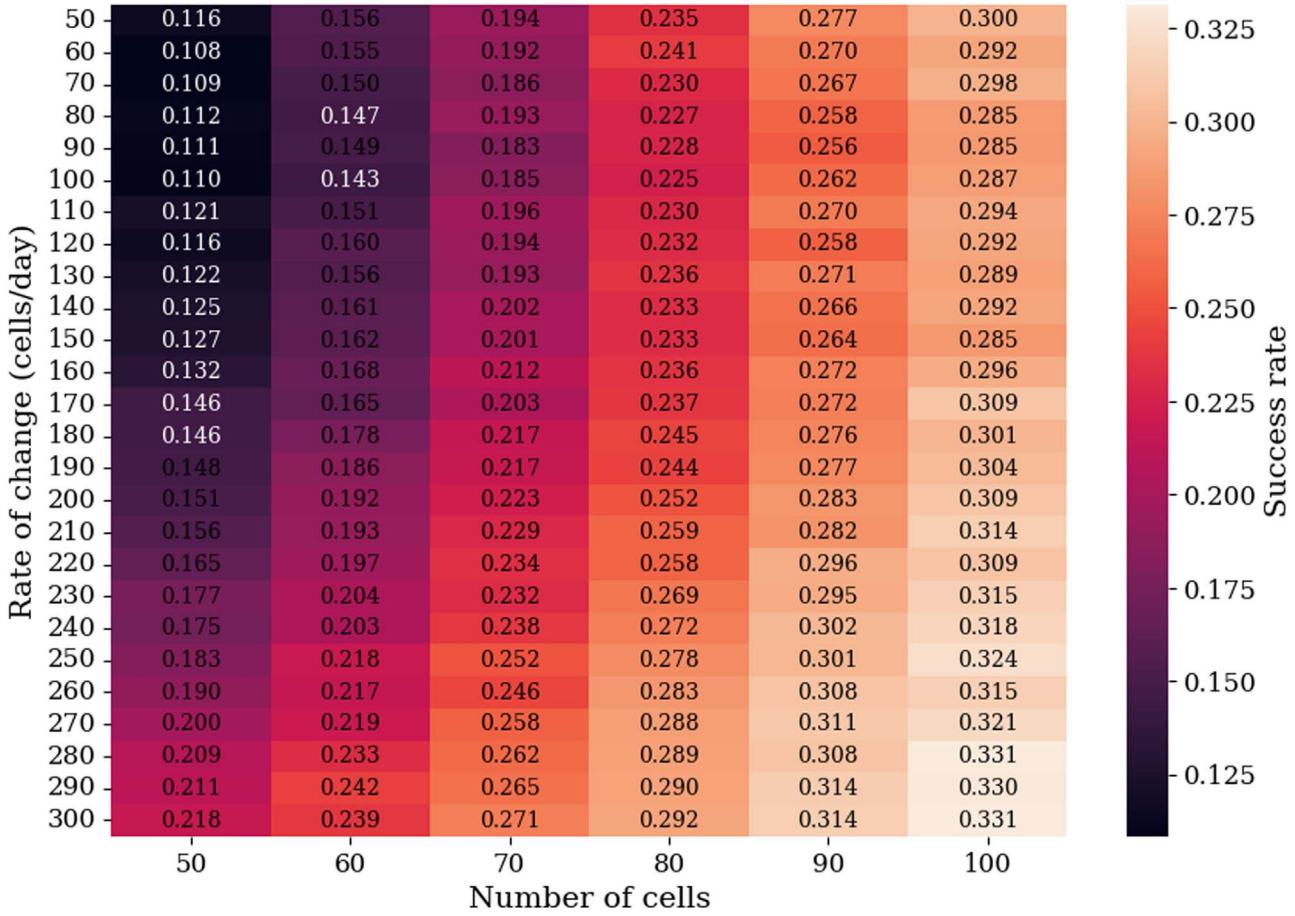

Figure 9. Parameter space of the random-walk simulations. The color bar shows the fraction of successful simulations that reproduce the median polarization degree within 10% of the observed value.

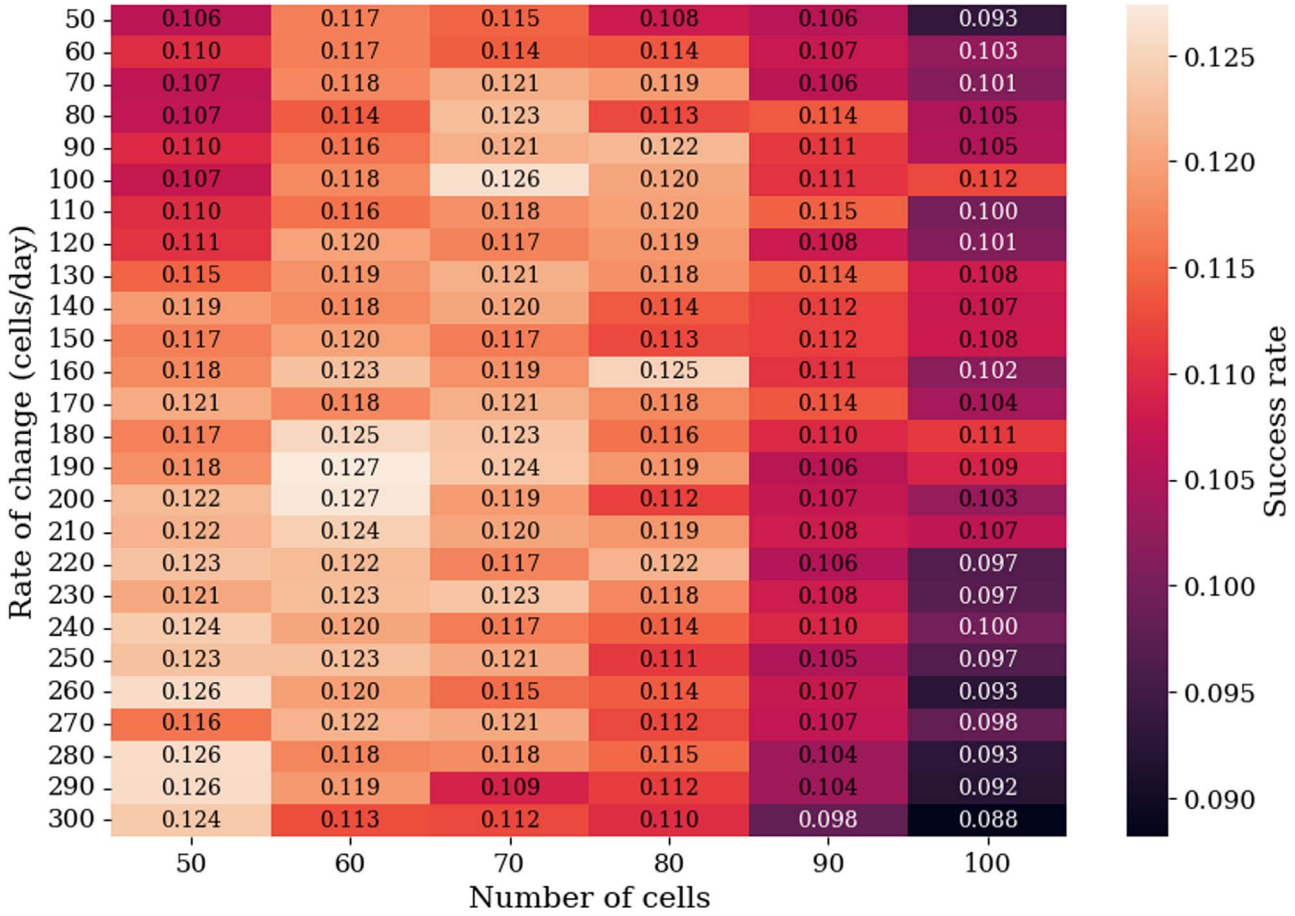

Figure 10. Parameter space of the random-walk simulations. The color bar shows the fraction of successful simulations that reproduce the interquartile range of the polarization degree within 10% of the observed value.

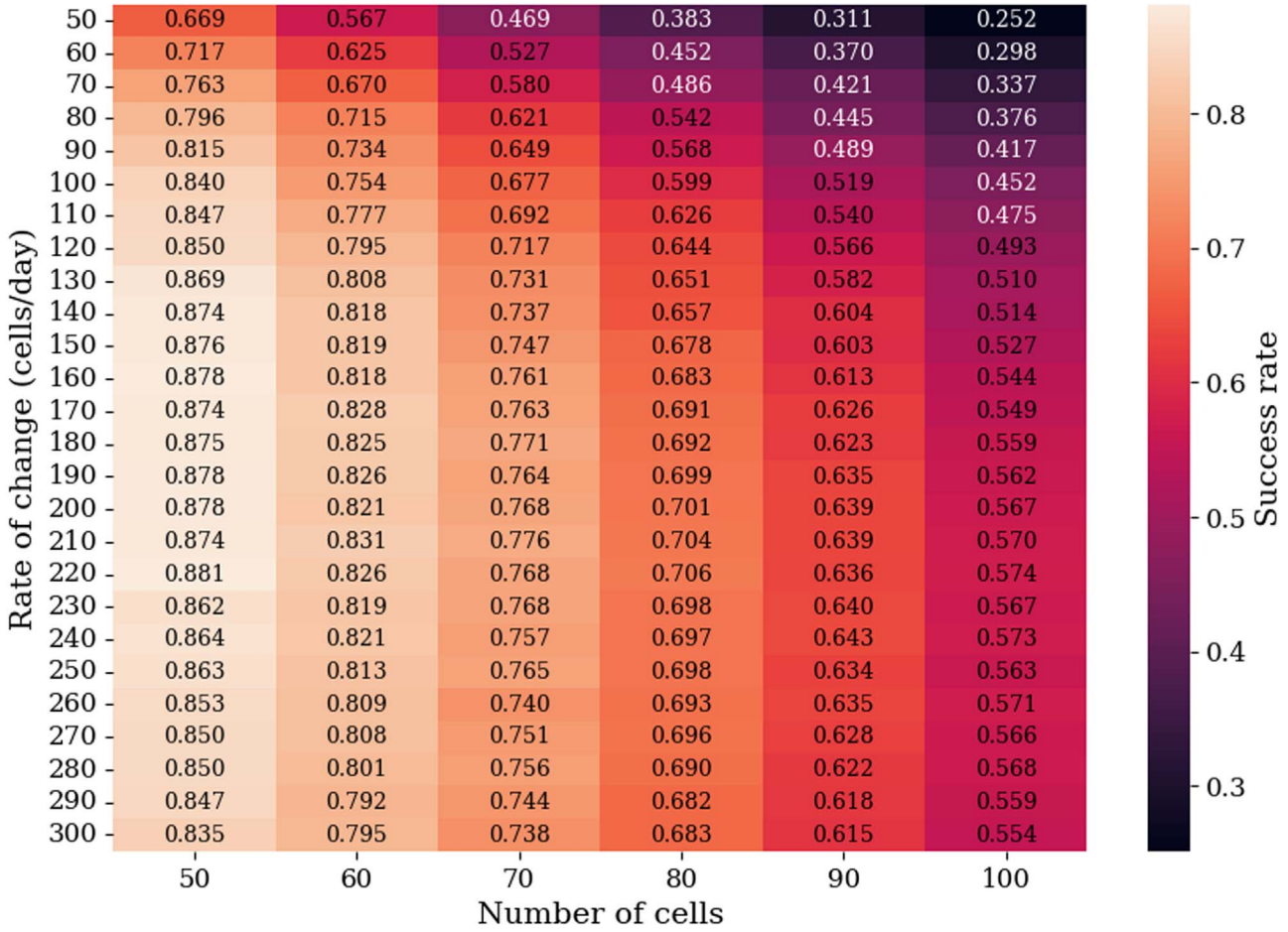

Figure 11. Parameter space of the random-walk simulations. The color bar shows the fraction of successful simulations that reproduce an equal or larger amplitude rotation of the polarization angle compared with the observed value.

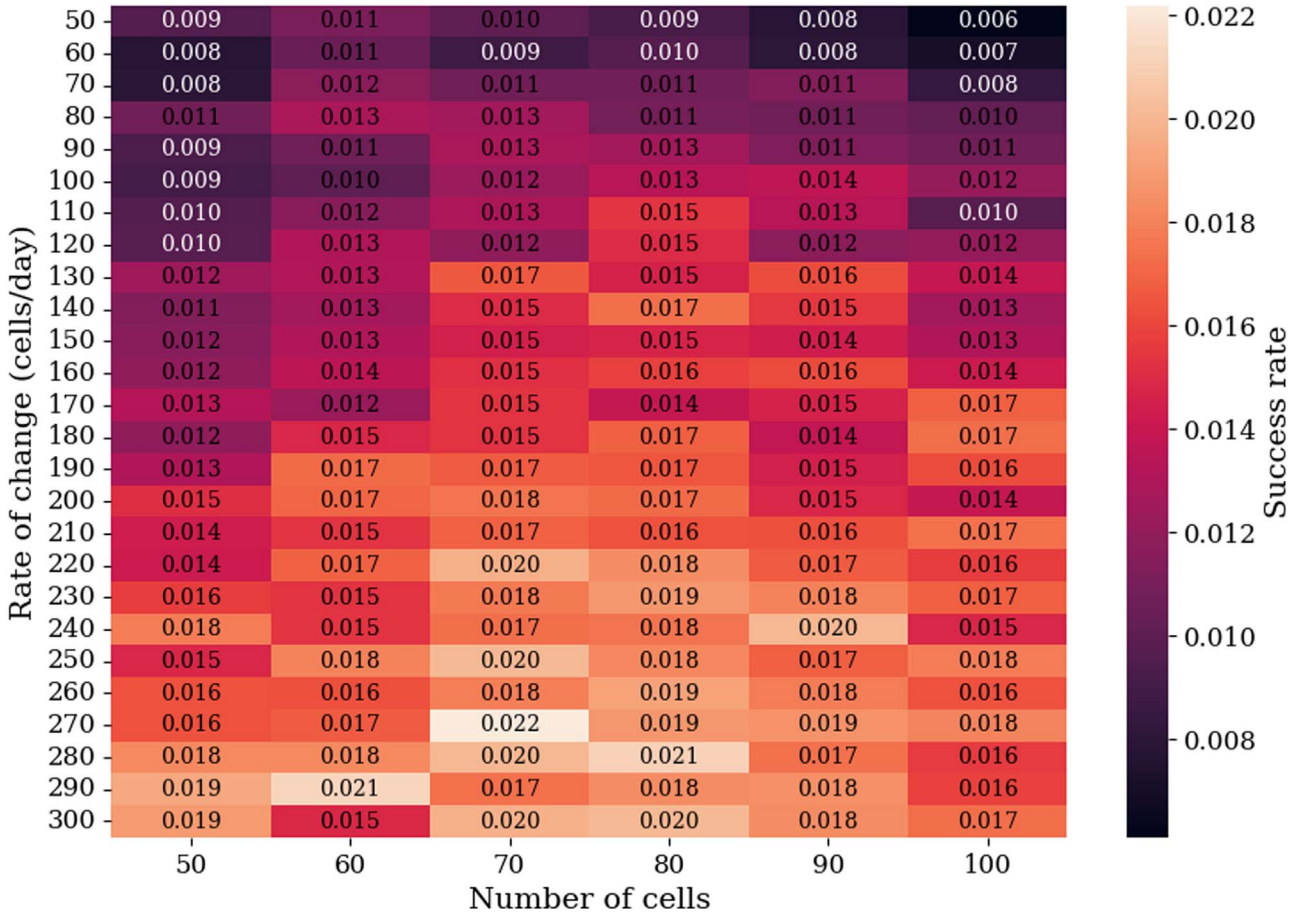

Figure 12. Parameter space of the random-walk simulations. The color bar shows the fraction of successful simulations that reproduce the observed median and interquartile range of the polarization degree (within 10%) and show an equal or larger amplitude rotation of the polarization angle relative to the observed value.

ORCID iDs

W. Peter Maksym https://orcid.org/0000-0002-2203-7889
Ioannis Liodakis https://orcid.org/0000-0001-9200-4006
M. Lynne Saade https://orcid.org/0000-0001-7163-7015
Dawoon E. Kim https://orcid.org/0000-0001-5717-3736
Riccardo Middei https://orcid.org/0000-0001-9815-9092
Laura Di Gesu https://orcid.org/0000-0002-5614-5028
Sebastian Kiehlmann https://orcid.org/0000-0001-6314-9177
Iván Agudo https://orcid.org/0000-0002-3777-6182
Alan P. Marscher https://orcid.org/0000-0001-7396-3332
Steven R. Ehlert https://orcid.org/0000-0003-4420-2838
Svetlana G. Jorstad https://orcid.org/0000-0001-6158-1708
Philip Kaaret https://orcid.org/0000-0002-3638-0637
Herman L. Marshall https://orcid.org/0000-0002-6492-1293
Luigi Pacciani https://orcid.org/0000-0001-6897-5996
Matteo Perri https://orcid.org/0000-0003-3613-4409
Simonetta Puccetti https://orcid.org/0000-0002-2734-7835
Pouya M. Kouch https://orcid.org/0000-0002-9328-2750
Giacomo Bonnoli https://orcid.org/0000-0003-2464-9077
Juan Escudero https://orcid.org/0000-0002-4131-655X
José L. Gómez https://orcid.org/0000-0003-4190-7613
Beatriz Agís-González https://orcid.org/0000-0001-7702-8931
César Husillos https://orcid.org/0000-0001-8286-5443
Daniel Morcuende https://orcid.org/0000-0001-9400-0922
Vilppu Piirola https://orcid.org/0000-0003-0186-206X
Ryo Imazawa https://orcid.org/0000-0002-0643-7946
Yasushi Fukazawa https://orcid.org/0000-0002-0921-8837
Koji S. Kawabata https://orcid.org/0000-0001-6099-9539
Makoto Uemura https://orcid.org/0000-0002-7375-7405
Tsunefumi Mizuno https://orcid.org/0000-0001-7263-0296
Hiroshi Akitaya https://orcid.org/0000-0001-6156-238X
Callum McCall https://orcid.org/0000-0002-3375-3397
Helen E. Jermak https://orcid.org/0000-0002-1197-8501
George A. Borman https://orcid.org/0000-0002-7262-6710
Tatiana S. Grishina https://orcid.org/0000-0002-3953-6676
Vladimir A. Hagen-Thorn https://orcid.org/0000-0002-6431-8590
Evgenia N. Kopatskaya https://orcid.org/0000-0001-9518-337X
Elena G. Larionova https://orcid.org/0000-0002-2471-6500
Daria A. Morozova https://orcid.org/0000-0002-9407-7804
Sergey S. Savchenko https://orcid.org/0000-0003-4147-3851
Ivan S. Troitskiy https://orcid.org/0000-0002-4218-0148
Yulia V. Troitskaya https://orcid.org/0000-0002-9907-9876
Andrey A. Vasilyev https://orcid.org/0000-0002-8293-0214
Alexey V. Zhovtan https://orcid.org/0000-0002-8293-0214
Ioannis Myserlis https://orcid.org/0000-0003-3025-9497
Mark Gurwell https://orcid.org/0000-0003-0685-3621
Garrett Keating https://orcid.org/0000-0002-3490-146X
Ramprasad Rao https://orcid.org/0000-0002-1407-7944
Colt Pauley https://orcid.org/0009-0006-5434-0475

Emmanouil Angelakis https://orcid.org/0000-0001-7327-5441
Alexander Kraus https://orcid.org/0000-0002-4184-9372
Andrei V. Berdyugin https://orcid.org/0000-0002-9353-5164
Vadim Kravtsov https://orcid.org/0000-0002-7502-3173
Juri Poutanen https://orcid.org/0000-0002-0983-0049
Sincheol Kang https://orcid.org/0000-0002-0112-4836
Sang-Sung Lee https://orcid.org/0000-0002-6269-594X
Sang-Hyun Kim https://orcid.org/0000-0001-7556-8504
Whee Yeon Cheong https://orcid.org/0009-0002-1871-5824
Hyeon-Woo Jeong https://orcid.org/0009-0005-7629-8450
Chanwoo Song https://orcid.org/0009-0003-8767-7080
Lucio Angelo Antonelli https://orcid.org/0000-0002-5037-9034
Matteo Bachetti https://orcid.org/0000-0002-4576-9337
Luca Baldini https://orcid.org/0000-0002-9785-7726
Wayne H. Baumgartner https://orcid.org/0000-0002-5106-0463
Ronaldo Bellazzini https://orcid.org/0000-0002-2469-7063
Stefano Bianchi https://orcid.org/0000-0002-4622-4240
Stephen D. Bongiorno https://orcid.org/0000-0002-0901-2097
Raffaella Bonino https://orcid.org/0000-0002-4264-1215
Alessandro Brez https://orcid.org/0000-0002-9460-1821
Niccoló Bucciantini https://orcid.org/0000-0002-8848-1392
Fiamma Capitanio https://orcid.org/0000-0002-6384-3027
Simone Castellano https://orcid.org/0000-0003-1111-4292
Elisabetta Cavazzuti https://orcid.org/0000-0001-7150-9638
Chien-Ting Chen https://orcid.org/0000-0002-4945-5079
Stefano Ciprini https://orcid.org/0000-0002-0712-2479
Enrico Costa https://orcid.org/0000-0003-4925-8523
Alessandra De Rosa https://orcid.org/0000-0001-5668-6863
Ettore Del Monte https://orcid.org/0000-0002-3013-6334
Niccoló Di Lalla https://orcid.org/0000-0002-7574-1298
Alessandro Di Marco https://orcid.org/0000-0003-0331-3259
Immacolata Donnarumma https://orcid.org/0000-0002-4700-4549
Victor Doroshenko https://orcid.org/0000-0001-8162-1105
Michal Dovčiak https://orcid.org/0000-0003-0079-1239
Teruaki Enoto https://orcid.org/0000-0003-1244-3100
Yuri Evangelista https://orcid.org/0000-0001-6096-6710
Sergio Fabiani https://orcid.org/0000-0003-1533-0283
Riccardo Ferrazzoli https://orcid.org/0000-0003-1074-8605
Javier A. Garcia https://orcid.org/0000-0003-3828-2448
Shuichi Gunji https://orcid.org/0000-0002-5881-2445
Jeremy Heyl https://orcid.org/0000-0001-9739-367X
Wataru Iwakiri https://orcid.org/0000-0002-0207-9010
Vladimir Karas https://orcid.org/0000-0002-5760-0459
Fabian Kislat https://orcid.org/0000-0001-7477-0380
Jeffery J. Kolodziejczak https://orcid.org/0000-0002-0110-6136
Henric Krawczynski https://orcid.org/0000-0002-1084-6507
Fabio La Monaca https://orcid.org/0000-0001-8916-4156
Luca Latronico https://orcid.org/0000-0002-0984-1856
Simone Maldera https://orcid.org/0000-0002-0698-4421
Alberto Manfreda https://orcid.org/0000-0002-0998-4953
Frédéric Marin https://orcid.org/0000-0003-4952-0835
Andrea Marinucci https://orcid.org/0000-0002-2055-4946
Francesco Massaro https://orcid.org/0000-0002-1704-9850
Giorgio Matt https://orcid.org/0000-0002-2152-0916
Fabio Muleri https://orcid.org/0000-0003-3331-3794
Michela Negro https://orcid.org/0000-0002-6548-5622
C.-Y. Ng https://orcid.org/0000-0002-5847-2612
Stephen L. O'Dell https://orcid.org/0000-0002-1868-8056
Nicola Omodei https://orcid.org/0000-0002-5448-7577
Chiara Oppedisano https://orcid.org/0000-0001-6194-4601
Alessandro Papitto https://orcid.org/0000-0001-6289-7413
George G. Pavlov https://orcid.org/0000-0002-7481-5259
Abel Lawrence Peirson https://orcid.org/0000-0001-6292-1911
Melissa Pesce-Rollins https://orcid.org/0000-0003-1790-8018
Pierre-Olivier Petrucci https://orcid.org/0000-0001-6061-3480
Maura Pilia https://orcid.org/0000-0001-7397-8091
Andrea Possenti https://orcid.org/0000-0001-5902-3731
Brian D. Ramsey https://orcid.org/0000-0003-1548-1524
John Rankin https://orcid.org/0000-0002-9774-0560
Ajay Ratheesh https://orcid.org/0000-0003-0411-4243
Oliver J. Roberts https://orcid.org/0000-0002-7150-9061
Roger W. Romani https://orcid.org/0000-0001-6711-3286
Carmelo Sgró https://orcid.org/0000-0001-5676-6214
Patrick Slane https://orcid.org/0000-0002-6986-6756
Paolo Soffitta https://orcid.org/0000-0002-7781-4104
Gloria Spandre https://orcid.org/0000-0003-0802-3453
Douglas A. Swartz https://orcid.org/0000-0002-2954-4461
Toru Tamagawa https://orcid.org/0000-0002-8801-6263
Fabrizio Tavecchio https://orcid.org/0000-0003-0256-0995
Roberto Taverna https://orcid.org/0000-0002-1768-618X
Yuzuru Tawara https://orcid.org/0000-0002-9443-6774
Allyn F. Tennant https://orcid.org/0000-0002-9443-6774
Nicholas E. Thomas https://orcid.org/0000-0003-0411-4606
Francesco Tombesi https://orcid.org/0000-0002-6562-8654
Alessio Trois https://orcid.org/0000-0002-3180-6002
Sergey S. Tsygankov https://orcid.org/0000-0002-9679-0793
Roberto Turolla https://orcid.org/0000-0003-3977-8760
Jacco Vink https://orcid.org/0000-0002-4708-4219
Martin C. Weisskopf https://orcid.org/0000-0002-5270-4240
Kinwah Wu https://orcid.org/0000-0002-7568-8765
Fei Xie https://orcid.org/0000-0002-0105-5826
Silvia Zane https://orcid.org/0000-0001-5326-880X

References

Abdo, A. A., Ackermann, M., Ajello, M., et al. 2010, Natur, 463, 919
Ajello, M., Baldini, L., Ballet, J., et al. 2022, ApJS, 263, 24
Akitaya, H., Moritani, Y., Ui, T., et al. 2014, Proc. SPIE, 9147, 91474O
Angelakis, E., Hovatta, T., Blinov, D., et al. 2016, MNRAS, 463, 3365
Arnaud, K. A. 1996, in ASP Conf. Ser. 101, Astronomical Data Analysis Software and Systems V, ed. G. H. Jacoby & J. Barnes (San Francisco, CA: ASP), 17
Baldini, L., Bucciantini, N., Lalla, N. D., et al. 2022, SoftX, 19, 101194
Baloković, M., Paneque, D., Madejski, G., et al. 2016, ApJ, 819, 156
Berdyugin, A., Piirola, V., & Poutanen, J. 2019, in Astrophysics and Space Science Library, Astronomical Polarisation from the Infrared to Gamma Rays, ed. R. Mignani et al., Vol. 460 (Berlin: Springer), 33

Berdyugin, A. V., Berdyugina, S. V., & Piirola, V. 2018, Proc. SPIE, 10702, 107024Z
Bharathan, A. M., Stalin, C. S., Sahayanathan, S., et al. 2024, ApJ, 975, 185
Blandford, R., Meier, D., & Readhead, A. 2019, ARA&A, 57, 467
Blinov, D., Pavlidou, V., Papadakis, I., et al. 2015, MNRAS, 453, 1669
Blinov, D., Pavlidou, V., Papadakis, I., et al. 2018, MNRAS, 474, 1296
Blinov, D., Jorstad, S. G., Larionov, V. M., et al. 2021, MNRAS, 505, 4616
Bolis, F., Sobacchi, E., & Tavecchio, F. 2024, A&A, 690, A14
Chen, C.-T. J., Liodakis, I., Middei, R., et al. 2024, ApJ, 974, 50
Di Gesu, L., Donnarumma, I., Tavecchio, F., et al. 2022, ApJL, 938, L7
Di Gesu, L., Marshall, H. L., Ehlert, S. R., et al. 2023, NatAs, 7, 1245
Ehlert, S. R., Ferrazzoli, R., Marinucci, A., et al. 2022, ApJ, 935, 116
Ehlert, S. R., Liodakis, I., Middei, R., et al. 2023, ApJ, 959, 61
Errando, M., Liodakis, I., Marscher, A. P., et al. 2024, ApJ, 963, 5
Escudero, J., & Morcuende, D. 2023, juanep97/iop4 v:0.1.0, Zenodo, doi:10.5281/zenodo.10222722
Escudero Pedrosa, J., Agudo, I., Morcuende, D., et al. 2024, AJ, 168, 84
Hosking, D. N., & Sironi, L. 2020, ApJL, 900, L23
Hovatta, T., & Lindfors, E. 2019, NewAR, 87, 101541
Hovatta, T., Lindfors, E., Blinov, D., et al. 2016, A&A, 596, A78
Jermak, H., Steele, I. A., & Smith, R. J. 2016, Proc. SPIE, 9908, 99084I
Jorstad, S. G., Marscher, A. P., Larionov, V. M., et al. 2010, ApJ, 715, 362
Jorstad, S. G., Marscher, A. P., Morozova, D. A., et al. 2017, ApJ, 846, 98
Kang, S., Lee, S.-S., & Byun, D.-Y. 2015, JKAS, 48, 257
Kawabata, K. S., Okazaki, A., Akitaya, H., et al. 1999, PASP, 111, 898
Kiehlmann, S., Blinov, D., Pearson, T. J., & Liodakis, I. 2017, MNRAS, 472, 3589
Kiehlmann, S., Blinov, D., Liodakis, I., et al. 2021, MNRAS, 507, 225
Kim, D. E., Di Gesu, L., Liodakis, I., et al. 2024a, A&A, 681, A12
Kim, D. E., Di Gesu, L., Marin, F., et al. 2024b, Galax, 12, 20
Kouch, P. M., Liodakis, I., Fenu, F., et al. 2025, A&A, 695, A99
Kouch, P. M., Liodakis, I., Middei, R., et al. 2024, A&A, 689, A119
Kraus, A., Krichbaum, T. P., Wegner, R., et al. 2003, A&A, 401, 161
Krawczynski, H., Muleri, F., Dovčiak, M., et al. 2022, Sci, 378, 650
Larionov, V. M., Jorstad, S. G., Marscher, A. P., et al. 2008, A&A, 492, 389
Liodakis, I., Blinov, D., Jorstad, S. G., et al. 2020, ApJ, 902, 61
Liodakis, I., Hovatta, T., Huppenkothen, D., et al. 2018, ApJ, 866, 137
Liodakis, I., Marscher, A. P., Agudo, I., et al. 2022, Natur, 611, 677
Lisalda, L., et al. 2025, MNRAS, submitted
Madsen, K. K., Harrison, F. A., Markwardt, C. B., et al. 2015, ApJS, 220, 8
Manchester, R. N. 1972, ApJ, 172, 43
Marrone, D. P., & Rao, R. 2008, Proc. SPIE, 7020, 70202B
Marscher, A. P. 2014, ApJ, 780, 87
Marscher, A. P., & Gear, W. K. 1985, ApJ, 298, 114
Marscher, A. P., & Jorstad, S. G. 2021, Galax, 9, 27
Marscher, A. P., Jorstad, S. G., D'Arcangelo, F. D., et al. 2008, Natur, 452, 966
Marscher, A. P., Jorstad, S. G., Larionov, V. M., et al. 2010, ApJL, 710, L126
Marshall, H. L., Liodakis, I., Marscher, A. P., et al. 2024, ApJ, 972, 74
Massaro, E., Perri, M., Giommi, P., Nesci, R., & Verrecchia, F. 2004, A&A, 422, 103
Middei, R., Giommi, P., Perri, M., et al. 2022, MNRAS, 514, 3179
Middei, R., Perri, M., Puccetti, S., et al. 2023, ApJL, 953, L28
Myserlis, I., Angelakis, E., Kraus, A., et al. 2018, A&A, 609, A68
Nilsson, K., Pasanen, M., Takalo, L. O., et al. 2007, A&A, 475, 199
Nilsson, K., Lindfors, E., Takalo, L. O., et al. 2018, A&A, 620, A185
Otero-Santos, J., Piirola, V., Escudero Pedrosa, J., et al. 2024, AJ, 167, 137
Peirson, A. L., Negro, M., Liodakis, I., et al. 2023, ApJL, 948, L25
Piirola, V. 1973, A&A, 27, 383
Piirola, V., Kosenkov, I. A., Berdyugin, A. V., Berdyugina, S. V., & Poutanen, J. 2021, AJ, 161, 20
Ramaprakash, A. N., Rajarshi, C. V., Das, H. K., et al. 2019, MNRAS, 485, 2355
Shrestha, M., Steele, I. A., Piascik, A. S., et al. 2020, MNRAS, 494, 4676
Tavecchio, F., Landoni, M., Sironi, L., & Coppi, P. 2018, MNRAS, 480, 2872
Weaver, Z. R., Jorstad, S. G., Marscher, A. P., et al. 2022, ApJS, 260, 12
Weisskopf, M. C., Soffitta, P., Baldini, L., et al. 2022, JATIS, 8, 026002
Zhang, H., Li, H., Guo, F., & Taylor, G. 2017, ApJ, 835, 125
Zhang, H., Li, X., Giannios, D., et al. 2020, ApJ, 901, 149